HIPPARCHOS

The Hellenic Astronomical Society Newsletter

Volume 3, Issue 9

ISSN: 1790-9252

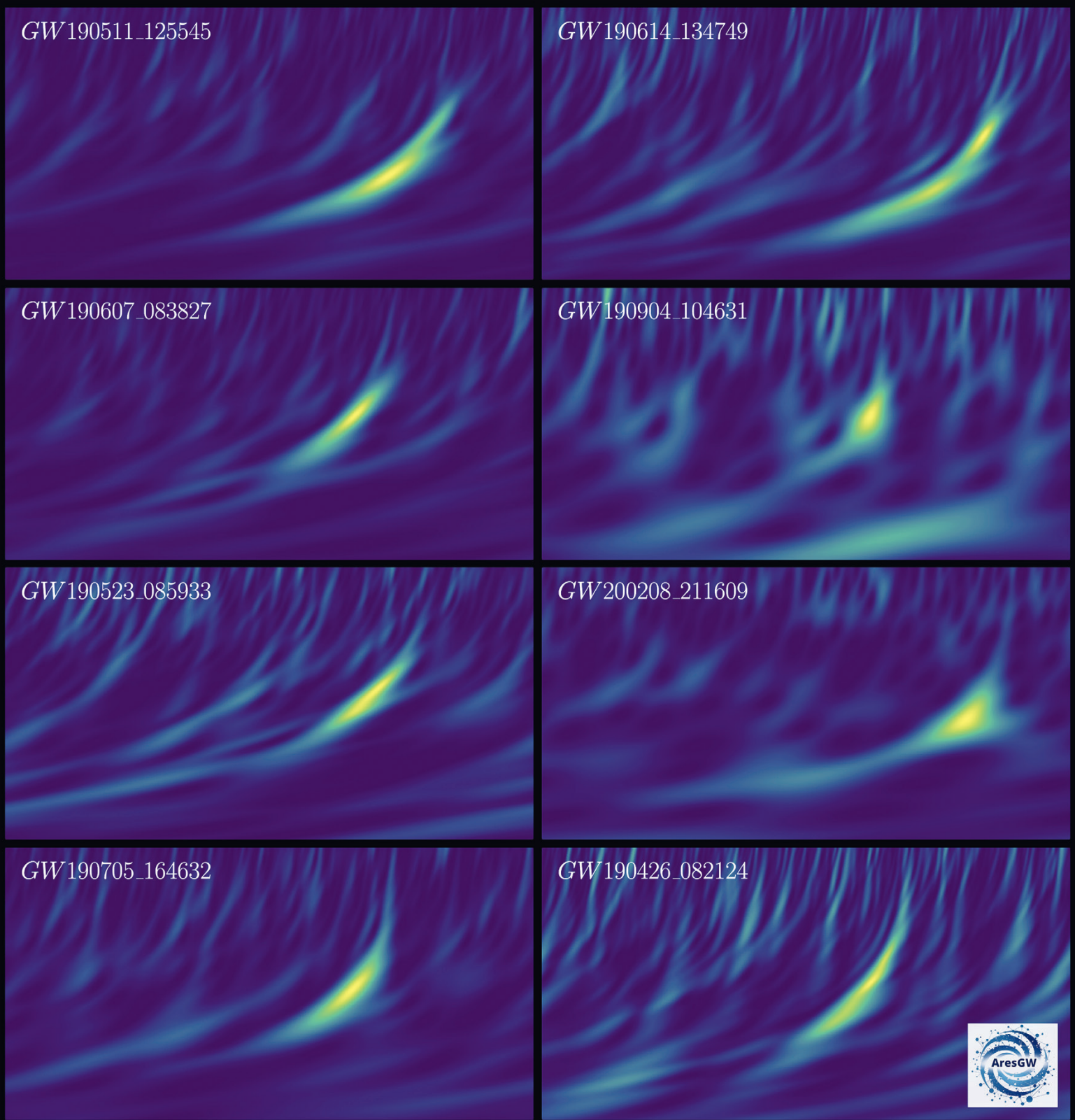

HIPPARCHOS

Volume 3, Issue 9 • June 2025

ISSN: 1790-9252

Hipparchos is the official newsletter of the Hellenic Astronomical Society. It publishes review papers, news and comments on topics of interest to astronomers, including matters concerning members of the Hellenic Astronomical Society.

Contact person

Georgios Balasis
Institute for Astronomy, Astrophysics, Space Applications and Remote Sensing (IAASARS), National Observatory of Athens (NOA)
Lofos Nymphon, PO Box 20048, 11810, Athens
Tel: +30-210 349 0885
E-mail: gbalasis@noa.gr

Printed by ZITI Publications • www.ziti.gr

Contents

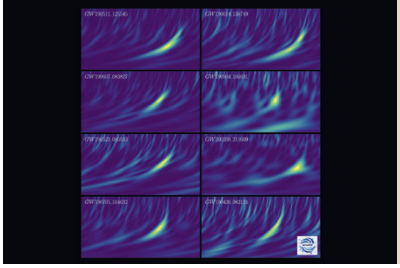

Cover Image:

Spectrograms of the eight new gravitational wave detections found with AresGW.
(Koloniari and Stergioulas, this issue)

Message from the President

Last year marked the election of our new Governing Council. I would like to extend my sincere congratulations to all members elected to serve in the 2024–2026 term. I am especially pleased to recognize and thank the three members —Dr. G. Balasis, Prof. M. Petropoulou, and Dr. A. Papaioannou— who were reelected for a second term. Their continued commitment reflects the trust and respect they have earned within our community.

I also wish to express my appreciation to the three outgoing Council members — Prof. K. Gourgouliatos, Dr. E. Koulouridis, and Prof. K. Tassis. Their long-standing service and dedication have played a vital role in advancing the mission and impact of the Society.

A special word of thanks goes to our outgoing President, Prof. V. Charmandaris, whose leadership over the past two terms has helped guide the Society through a period of growth and increased visibility, both nationally and internationally. His contributions and steady leadership are highly valued.

At the same time, I am delighted to welcome the three newly elected members to the Council —Dr. I. Antoniadis, Prof. V. Archontis, and Prof. I. Golias. Their perspectives and enthusiasm will positively contribute to the work of the Council.

It is a great honor to serve as the President of our Society for the 2024–2026 term. I look forward to building on the strong foundation laid by my predecessors and esteemed colleagues, and to working collaboratively with the new Council to further the mission of the Hellenic Astronomical Society.

The current issue of *Hipparchos* is the first I have the privilege of introducing as President of our Society. It continues the well-established tradition of presenting a series of high-quality articles that span the full spectrum of astrophysics and space physics — from galaxy evolution and the distant universe to the near-Earth space environment and the complex interactions between the solar wind and our planet's magnetic field.

It features three articles focused on emerging and rapidly expanding fields: two dedicated to gravitational-wave astronomy, and one to TeV astronomy with the Cherenkov Telescope Array Observatory. In addition, two articles explore topics related to the near-Earth space environment — one on space weather and another on near-Earth objects.

The current Governing Council has also introduced a new feature: *Hipparchos* will now include short articles highlighting key results from major research projects —such as those funded by the European Research Council— that have been carried out at Greek institutions. In this framework, the present issue includes two such reports: one by Dr. A. Bonanos on the outcomes of the ERC-funded ASSESS project, completed in 2024, and another by Prof. K. Tassis on the findings from the ERC-funded PASIPHAE project, also concluded in 2024.

I would like to sincerely thank all contributing authors for preparing their articles in a way that is both accessible to non-specialists and scientifically robust. In particular, I wish to acknowledge Dr. George Balasis, Vice President of our Society, whose dedicated efforts were instrumental in bringing this issue of *Hipparchos* to publication.

I am confident that readers will enjoy this collection of articles. This issue will be distributed during the 17th Conference of Hel.A.S., taking place in Patras from June 30th to July 2nd, 2025.

Despina Hatzidimitriou
President of Hel.A.S.

Gravitational Wave Astronomy with LISA. Entering the mHz regime

by **Nikolaos Karnesis** & **Nikolaos Stergioulas**

Department of Physics, Aristotle University of Thessaloniki

Abstract

We explore the transformative potential of the Laser Interferometer Space Antenna (LISA) in gravitational wave astronomy and the significant role of advanced Bayesian Data Analysis methods, such as `Eryn` and `Erebor`, co-developed at the Aristotle University of Thessaloniki through ESA PRODEX and MSCA grants. We also discuss the current status and prospects of the LISA community in Greece.

1. Detecting Gravitational Waves in space

The past decade has witnessed the birth of Gravitational Wave (GW) Astronomy, a transformative field that probes the universe's most cataclysmic events through ripples in spacetime. The LIGO-Virgo-KAGRA (LVK) collaboration has already detected or issued significant alerts for more than 300 GW events that originated from compact binary coalescences [1, 2]. These detections have unveiled a rich population of stellar-mass black holes, confirmed the existence of neutron star mergers with electromagnetic counterparts, and tested general relativity in extreme gravitational regimes. The science output of LVK is so rich and novel, that more advanced and more sensitive ground detectors are being under development [3, 4]. All this momentum is very exciting for our field, because we are going to be able to "catch" more distant sources, and in a far grater rate than current capabilities allow for. At the same time, the possibility to study binary objects with both Gravitational and Electromagnetic (EM) radiation is also going to increase, with immense consequences for astronomy and fundamental physics. However, the sensitivity curves of even the planned 3rd-generation detectors, feature a sharp rise of the noise at low frequencies of a few Hz, which fundamentally prevents us from searching for GW signatures with longer wavelengths using gound-based detectors. This means that we are essentially "deaf" to GW sources that emit at frequencies below this limit or the early inspiral phase of compact binaries. This form of noise arises predominantly from terrestrial factors, such as seismic, Newtonian, or thermal noise [5]. While many strategies have been devised to mitigate them, complete eradication remains unachievable, underscoring the complementary role of space-based detectors in exploring massive and cosmological GW sources. Such a space-based observatory is LISA [6], which will bypass the low-frequency noise wall to access the millihertz range.

In space, the low-frequency noise wall at ~1Hz is no longer a problem, and thus we will have access to a wealth of new astrophysical and cosmological sources. A space-base observatory will be able to detect the mergers of supermassive black hole (SMBH) binaries with masses of $10^5 - 10^8$ solar masses at high redshifts (up to $z \sim 20$), which would essentially be an indirect observation of collisions of galaxies that drive SMBH growth, thus constraining models of hierarchical galaxy formation and active galactic nuclei evolution. At the same time it will capture the inspiral phase of *all* the stellar-mass binary systems (white dwarfs, neutron stars, and black holes) in our own Galaxy, offering a census of galactic binaries, which would allow us to test different stellar population synthesis and galaxy evolution models, including the role of dynamical interactions in star clusters.

Additionally, LISA will probe extreme mass-ratio inspirals (EMRIs), where stellar-mass compact objects orbit SMBHs, mapping spacetime around massive black holes to test general relativity with unprecedented precision. Cosmological sources, such as stochastic GW backgrounds from the early universe (e.g., inflation or phase transitions) and hypothetical cosmic strings, are also within LISA's reach, offering insights into physics beyond the Standard Model. Sensitivity to these diverse sources will revolutionize our understanding of galaxy assembly, black hole demographics, and the universe's first moments. Furthermore, the synergy of GW and EM observations will unravel compact object physics, test fundamental theories, and map cosmic evolution, cementing GW astronomy's role as a cornerstone of modern astrophysics. This is the new kind of science that the field is excited with.

1.1 The Laser Interferometer Space Antenna

The concept of the LISA mission first appeared in the early '80s, and was soon refined to the current triangular constellation of three spacecraft [7] (see figure 1). During the '90s, it was slowly established as a large joint ESA-NASA project, and was presented as a Large Class mission concept in the ESA Cosmic Vision 2015-2025 programme [8]. The road to a space GW telescope was initially "bumpy" [9], but after the first detection of GWs and the immense success of the LISA Pathfinder mission [10–12], in early 2024 ESA finally adopted the mission with NASA as its junior partner [6, 13, 14].

LISA is predicted to be a signal-dominated observatory, because it is going to detect a large number of overlapping GW signals across its sensitivity band. At the same time, in contrast to current ground-based detectors, LISA will measure different types of waveform from different types of sources, each with different duration and spectral shape (see figure 2). Thus, the scientific potential of LISA is expected to be significant and impactful and is therefore highly anticipated by the community. The rich science of LISA is captured by the so-called Scientific Objectives (SO) of the mission, which were defined in the Definition Study Report [6] published by ESA and collaborating institutions.

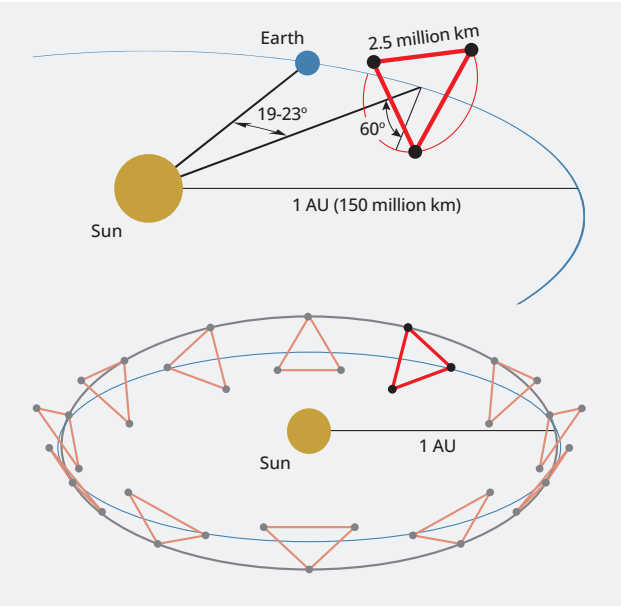

Figure 1: A cartoon depicting the LISA constellation and the spacecraft orbits. Figure from [15].

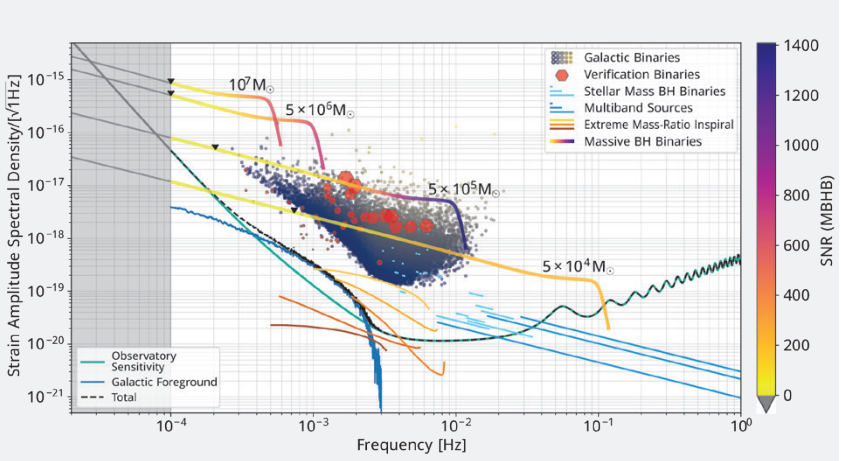

Figure 2: The LISA sensitivity and the different types of predicted sources. Figure from [6].

However, this abundance of potential sources creates a new challenge for our data analysis capabilities. The thousands of overlapping signals, together with our limited knowledge about the instrumental noise, create a situation where the data residuals are correlated with all waveform parameters for every type of source. This is only manageable by adopting a Bayesian *Global Fit* methodology, where all source and instrumental noises are inferred simultaneously from the data. This is by no means a trivial task, because the number of sources is not known a priori, and therefore a trans-dimensional technique is required. Since the parameter space is too large for grid-based methods, the data analysis effort has been concentrating on sampling methods such as Markov Chain Monte Carlo (MCMC). Nonetheless, developing advanced sampling techniques is not the main challenge; Robust noise models are required in order to disentangle overlapping signals and instrumental effects and ensure accurate source characterization. Furthermore, the success of LISA's science objectives will depend on international collaboration to refine these methods, leveraging simulated data challenges to prepare for the mission's launch in the mid-2030s.

1.2 Trans-dimensional sampling methods to the rescue

A significant development towards solving the Global Fit problem is `Eryn` [16], which was developed with the support of an ESA PRODEX grant to the GW group at the Aristotle University of Thessaloniki, in collaboration with researchers from the Albert-Einstein-Institut Potsdam, and APC/CNRS, Paris. `Eryn` is essentially a Reversible Jump MCMC (RJMCMC) on steroids. The "reversible" part of the algorithm denotes that it is capable of sampling both the dimensionality of the problem, as well as the parameters of the dynamical model (see figure 3). Specifically, `Eryn` leverages parallel tempering and ensemble sampling to improve convergence in high-dimensional spaces, making it well-suited for problems that exhibit dynamic and complex posterior surfaces. Concerning LISA, this capability allows us to efficiently explore the vast parameter space of overlapping GW sources while simultaneously modeling instrumental noise, a critical requirement for the Bayesian Global Fit scheme.

In general, RJMCMC methods are quite challenging to tune, usually resulting to a high-rejection rate at each iteration. With `Eryn`, we alleviate this issue by adopting techniques such as Parallel Tempering, where multiple chains are run in parallel, sampling "tempered" versions of the likelihood, where with increased temperatures T the likelihood surface appears more smoothened, and therefore easier to explore. The posterior p_T for temperature T is then written as

$$p_T(\theta|y) \propto p(y|\theta)^{1/T}\, p(\theta)\,, \quad (1)$$

were y is the given dataset, and $p(\theta)$ encapsulates any prior information we might have for the given parameters θ. At every iteration step of the MCMC procedure, a swap between chains of different temperatures is proposed, a technique which eventually prevents the chains to get stuck at local maxima of the posterior surface. In addition, each tempered posterior is sampled simultaneously by multiple MCMC walkers following the Ensemble Sampling technique [16]. We can also use the multiple walkers for building efficient proposal distributions which require minimal tuning from the user. All the above improvements allow for more efficient search of a very large and dynamical parameter space such as the one of the LISA data (See figure 4 for an example of using `Eryn` to disentangle multiple Gravitational Wave sources). We make `Eryn` available to the community as open-source software[1].

1. https://github.com/mikekatz04/Eryn

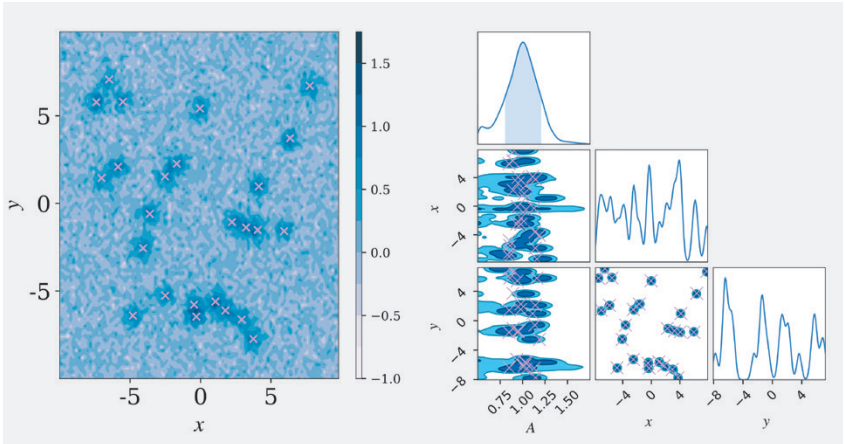

Figure 3: Example of using trans-dimensional sampling methods in order to recover both the unknown number of sources, and their corresponding parameters. The synthetic data consist of 25 injected 2D Gaussian pulses in Gaussian noise (left panel). In the right panel the 2D posterior densities for the parameters of the Gaussian peaks that were recovered with **Eryn** are shown. The crosses mark the "true" injected pulses. Figure from [16].

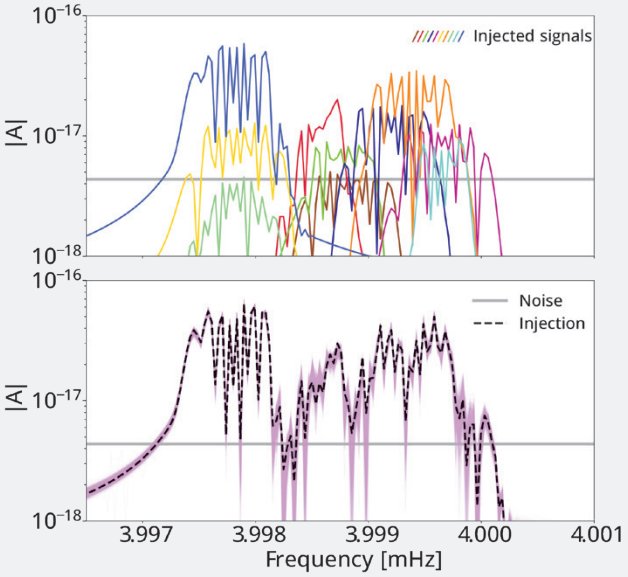

Figure 4: Fitting for an unknown number of Compact Galactic Binary sources using trans-dimensional Bayesian methods with **Eryn**. The total recovered signal (posterior predictive) is represented by the magenta band in the bottom panel. Figure from [16].

1.3 Erebor: Solving the Global Fit problem on GPUs

The modular structure of **Eryn** was leveraged in the new Global Fit analysis pipeline **Erebor** [17], which is the fruit of a collaboration between the Aristotle University of Thessaloniki, the Albert-Einstein-Institut in Potsdam, APC/CNRS and NASA, Huntsville. **Erebor** follows the Blocked Gibbs scheme shown in figure 5, where each type of source is fitted almost simultaneously, while the noise and residuals are being updated at each iteration. A significant improvement in the efficiency of the algorithm came after developing software supporting the usage of hardware Graphics Processing Units (GPUs). Using GPUs allowed us to compute a large number of waveforms simultaneously, thus greatly reducing computational resources. This setup, together with the versatility of **Eryn**, Which provides a user-friendly framework for building efficient proposals, even in combination with Machine Learning methods [18], allowed us to submit an analysis of a Mock LISA Data Challenge (see figure 6), and produce astrophysical catalogues of the recovered (or resolvable) sources. A total of 12000 Compact Binary Sources were resolved, while all injected massive Black Hole Binaries were recovered with great accuracy as expected, due to their high signal-to-noise ratio. In summary, with **Erebor** we sampled a 105- dimensional parameter space. The creation of **Erebor** was partially supported by the Marie Skłodowska-Curie Actions programme[2].

2. Current status of LISA and the community in Greece

The LISA mission was recently adopted by ESA [13], which means that we have the green light for the development of the actual instruments and various components of the observatory. At the same time, the LISA Science Team (LST) has been formed by ESA [20], which comprises experts in different fields relevant to LISA science. The LST is responsible for overseeing the smooth development of the observatory and ensuring that the maximum scientific potential is returned from the mission.

In addition, ESA and NASA have already established the two Ground Segments, the Distributed Data Processing Center (DDPC) for the European side, and the NASA Science Ground Segment (NSGS) for the US side. One of the main responsibilities of the DDPC and NSGS is to standardize prototypes, such as **Erebor**, which will analyze the LISA data and produce the final astrophysical catalogues to be published by ESA. Greece has already been approved to be part of the DDPC, and the effort is led by the GW Group at the Aristotle University of Thessaloniki. Our contribution focuses on AI-powered data analysis algorithms for the detection and characterization of the various GW signals [16, 17, 21].

In parallel, a coordination of interested researchers at the national level in Greece began in 2022, when the *First LISA in Greece Workshop* [22] took place at the Aristotle University of Thessaloniki, co-organized with the Hellenic Space Center[3]. Our main speakers included ESA and LISA Consortium representatives, such as O. Jennrich (LISA Project Scientist), M. Gehler (LISA Study Scientist), M. Hewitson (current LISA Mission & Performance Manager), and A. Petiteau (then chair of Data Processing Group), while the national scientific community and Space Industry ecosystem were also represented. The

2. MSCA Grant agreement No 101065596.
3. https://hsc.gov.gr/

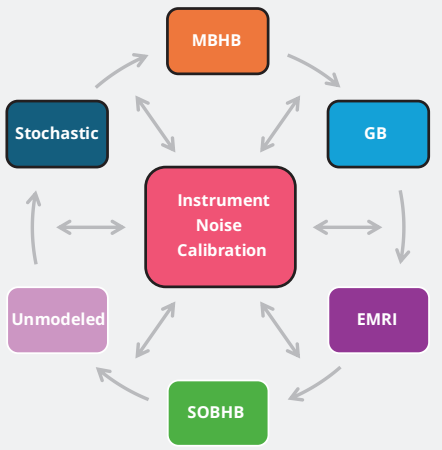

Figure 5: A cartoon of a Global Fit analysis strategy, following the Blocked Gibbs scheme in **Erebor**. Each source is analyzed simultaneously, while also updating the residual data. Figure from [17]

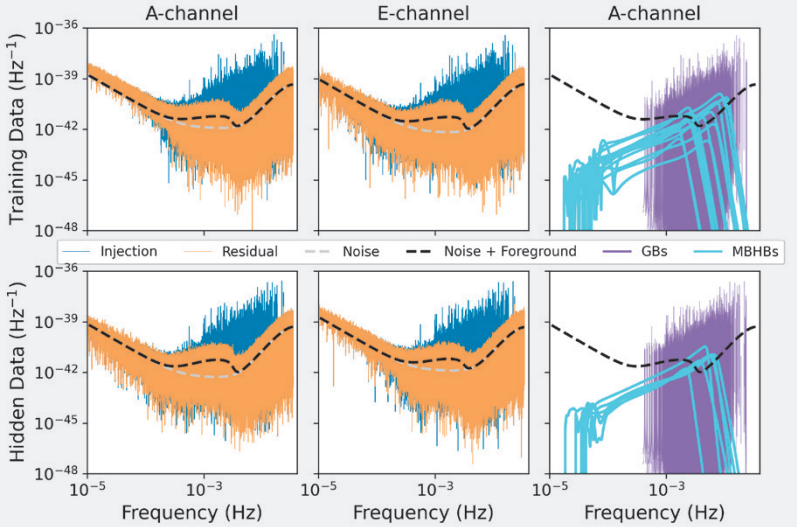

Figure 6: The **Erebor** Global Fit scheme recovering different types of signals in synthetic LISA data (Compact Galactic Binaries, Massive Black Holes, and stochastic signals). The two LISA TDI [19] data channels are shown. Figure from [17].

State was represented by the Secretary General of Telecommunications & Posts from the Ministry of Digital Governance. During the meeting, it was made clear that a joint national effort to contribute to the development and operations of the LISA mission can be accomplished. A relevant White Paper was published [23], which summarizes our national capabilities in science and technology concerning Gravitational Wave Astronomy in Space. As a result of this first LISA workshop in Greece, several new members joined the LISA Consortium, which currently undergoes a transformation to a new structure.

These are exciting times, because we have entered the final period of preparations before the launch of the highly-anticipated LISA mission. We anticipate that LISA will revolutionize the way we see our Universe, and we hope that our national community in Greece will play a significant role in the discoveries that will come with our new space-based Gravitational Wave observatory.

References

1. LIGO, Virgo, KAGRA Scientific collaboration, *GWTC-3: Compact Binary Coalescences Observed by LIGO and Virgo during the Second Part of the Third Observing Run*, *Phys. Rev. X* **13** (2023) 041039 [2111.03606].
2. LIGO Scientific Collaboration, "GraceDB: The Gravitational-Wave Candidate Event Database." https://gracedb.ligo.org/
3. A. Abac et al., *The Science of the Einstein Telescope*, 2503.12263.
4. M. Evans et al., *A Horizon Study for Cosmic Explorer: Science, Observatories, and Community*, 2109.09882.
5. M. Mantovani et al., *The challenge of low frequency sensitivity in ground-based GW detectors*, *EPJ Web Conf.* **319** (2025) 09002.
6. LISA collaboration, *LISA Definition Study Report*, 2402.07571.
7. J. Faller et al., *An antenna for laser gravitational-wave observations in space*, *Advances in Space Research* **9** (1989) 107.
8. *Cosmic vision: Space science for europe 2015-2025*, Tech. Rep. BR-247, European Space Agency (October, 2005).
9. E. Samuel Reich, *Europe makes do without NASA*, *Nature* (2011).
10. https://sci.esa.int/web/lisa-pathfinder
11. M. Armano et al., *Sub-femto-g free fall for space-based gravitational wave observatories: Lisa pathfinder results*, *Phys. Rev. Lett.* **116** (2016) 231101.
12. M. Armano et al., *Beyond the Required LISA Free-Fall Performance: New LISA Pathfinder Results down to 20 μHz*, *Phys. Rev. Lett.* **120** (2018) 061101.
13. https://www.esa.int/Science_Exploration/Space_Science/LISA/Capturing_the_ripples_of_spacetime_LISA_gets_go-ahead
14. eLISA collaboration, *The Gravitational Universe*, 1305.5720.
15. LISA collaboration, *Laser Interferometer Space Antenna*, 1702.00786.
16. N. Karnesis et al., *Eryn: A multi-purpose sampler for Bayesian inference*, *Mon. Not. Roy. Astron. Soc.* **526** (2023) 4814 [2303.02164].
17. M.L. Katz, N. Karnesis et al., *Eflcient GPU-accelerated multisource global fit pipeline for LISA data analysis*, *Phys. Rev. D* **111** (2025) 024060 [2405.04690].
18. N. Korsakova, S. Babak, M.L. Katz, N. Karnesis, S. Khukhlaev and J.R. Gair, *Neural density estimation for Galactic binaries in the LISA data analysis*, *Phys. Rev. D* **110** (2024) 104069 [2402.13701].
19. M. Tinto and S.V. Dhurandhar, *Time-delay interferometry*, *Living Rev. Rel.* **24** (2021) 1.
20. https://www.cosmos.esa.int/web/lisa/lisa-science-team
21. A.E. Koloniari et al., *New gravitational wave discoveries enabled by machine learning*, *Mach. Learn. Sci. Tech.* **6** (2025) 015054 [2407.07820].
22. https://indico.physics.auth.gr/e/lisa_gr_2022
23. N. Karnesis et al., *The Laser Interferometer Space Antenna mission in Greece White Paper*, *Int. J. Mod. Phys. D* **33** (2024) 2450027 [2209.04358].

Unveiling Gravitational Waves with Deep Learning: AresGW's New Discoveries

by **Alexandra Eleni Koloniari** & **Nikolaos Stergioulas**
Department of Physics, Aristotle University of Thessaloniki

Abstract

Machine learning is increasingly integral to gravitational wave astronomy, and we highlight AresGW — a deep learning algorithm developed at the Aristotle University of Thessaloniki — that achieved the first machine-learning-based coincident detections of eight new binary black hole mergers in LIGO O3 data.

1. Introduction

Gravitational waves (GWs) offer a unique observational window into the universe's most energetic and cataclysmic events. These ripples in spacetime, generated by the acceleration of massive objects such as merging black holes or neutron stars, provide a novel probe into the universe's most violent phenomena. Their detection relies on a combination of high-precision instrumentation and increasingly sophisticated data analysis strategies, with machine learning (ML) emerging as a promising tool to enhance sensitivity and efficiency in processing the growing data volume.

Since the advent of GW astronomy, the LIGO-Virgo Collaboration — later joined by KAGRA — has completed a series of observation runs (O1–O3), yielding about 90 confirmed events documented in the GWTC catalogs [1–4]. Additional detections have been reported by independent pipelines in the OGC [5–8] and IAS [9–11] catalogs. The bulk of detections comprises binary black hole mergers; however, rarer neutron star systems have also been observed, enriching the parameter space available for algorithmic benchmarking and validation. As the LVK collaboration moves through the fourth observation period (O4) with over 200 new significant alerts reported, so far, the computational challenges associated with conventional matched filtering methods — especially for complex systems with spin-precession or possible beyond-GR signatures — are becoming increasingly evident.

In response, ML approaches have proliferated in the field, especially in glitch classification, surrogate waveform model construction, and rapid parameter estimation, as documented in recent surveys [12–15]. A notable milestone in this context was the Machine-Learning Gravitational-Wave Mock Data Challenge (MLGWSC- 1) [16], which established a rigorous comparative setting for ML-based pipelines, using synthetic data sets based on real detector noise. In this challenge, the Virgo- AUTH implementation (a precursor to AresGW model 2) emerged as the leading algorithm to detect binary black hole mergers with component masses m_1 and m_2 in the range of 7–50 $M_\odot$, a mass regime that encompasses roughly 70% of GWTC-3 sources [4].

The Virgo-AUTH code was the result of the collaboration between members of the Virgo Gravitational Waves group at the Department of Physics of the Aristotle University of Thessaloniki and the Computational Intelligence and Deep Group at the Informatics Department of the same University[1]. These promising results spurred further development, culminating in AresGW model 1 [17, 18], which marked a significant advance, allowing us to achieve a comparable or better performance than standard (nonoptimized for this mass range) traditional matched filtering setups.

Building on this foundation, AresGW model 2 was recently introduced in [19], incorporating several enhancements aimed at improving detection robustness and astrophysical interpretability. Key aspects include the adoption of a logarithmic ranking statistic and the first calculation of the astrophysical probability, p_{astro}, for candidate events using a ML-based pipeline. Applying this model to O3 data, we identified *eight previously unreported events*, all with $p_{\text{astro}} \geq 0.5$ and a cumulative astrophysical probability of 5.94. This constitutes the *first instance of new coincident event detections by a ML-based algorithm*.

Several factors contribute to why these events were not reported by other pipelines, yet successfully identified by AresGW model 2, the most significant being its distinctive ability to perform a joint analysis of time-series data from both LIGO detectors, directly yielding a single ranking statistic. This allows the model to exploit interdetector correlations and extract subtle features that may evade traditional matched-filtering analyses that initially run on individual detectors and then search for coincident events.

For conciseness, we adopt the convention of referring to the most recent version — AresGW model 2 — as *AresGW* in what follows. Earlier variants, namely *Virgo-AUTH* [16] and *AresGW model 1* [17], will be explicitly cited by their respective names.

1. Specifically, the initial version of the code was developed primarily by Dr. Paraskevi Nousi (now at the Swiss Data Science Center - ETH).

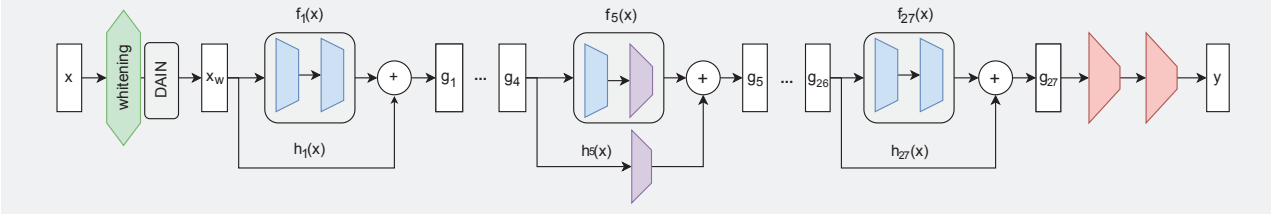

Figure 1: Main features of the 1-D ResNet architecture used in AresGW (see text for details). Figure from [17].

2. The AresGW Code

In recent years, a variety of neural network architectures, including convolutional neural networks, autoencoders, and hybrid models, have been tested on synthetic data sets to evaluate their potential in gravitational wave detection (see [12–14] for reviews). Among these, the ResNet architecture, first applied to synthetic data in real noise in [16, 17], has demonstrated state-of-the-art performance for detection tasks, becoming the current standard in the field. In the following, we detail the design of AresGW's ResNet model, as well as the associated preprocessing pipeline and training methodology.

2.1 Residual Network Architecture and Training Strategies

Residual neural networks (ResNets) [20] use skip connections to facilitate gradient flow, address vanishing gradients and allow effective training of deeper models compared to standard convolutional neural networks (CNNs). Greater depth has been linked to improved abstraction and performance in various classification tasks, including signal detection.

Specifically AresGW, uses a 54-layer 1-D ResNet architecture designed to classify 1-second segments from the two aLIGO detectors (thus 2×2048 samples) as either noise or containing a signal, assigning an output value between 0 and 1 that can be used as a ranking statistic. The network comprises 27 residual blocks, each built from two convolutional layers with varying kernel sizes. Dimensionality is reduced via strided convolutions in blocks 5, 8, 11, 14, and 17, with corresponding modifications to the residual paths. The output of each residual block is expressed as:

$$\mathbf{g} = f(\mathbf{x}) + h(\mathbf{x}), \qquad (1)$$

where $f(\mathbf{x})$ is a two-layer convolutional block and $h(\mathbf{x})$ is either an identity mapping or a strided convolution. Each convolution is followed by batch normalization and ReLU activation. Two final convolutional layers reduce the output to a two-channel prediction representing the binary classification targets. Fig. 1 illustrates the main features of this architecture.

Due to the non-stationary nature of the detector noise, *Deep Adaptive Input Normalization* (DAIN) [21] was applied as a preprocessing step. Originally developed for non-stationary time-series tasks (like financial forecasting), DAIN adaptively normalizes input segments based on their statistical properties, improving robustness across varying noise conditions.

Training follows a *curriculum learning* scheme based on the signal-to-noise ratio (SNR) of each training sample. The network is first exposed to high-SNR signals and gradually trained on weaker injections. To reduce computational cost, an efficient approximation of the SNR is used (see [17] for details). During inference, the trained neural network simultaneously processes data segments from both LIGO detectors using a 0.1-second sliding window, producing a single ranking statistic per segment pair to indicate the probability of a gravitational wave signal. Triggers within 0.3 seconds are clustered into single events to mitigate redundant detections and reduce false-positive rates.

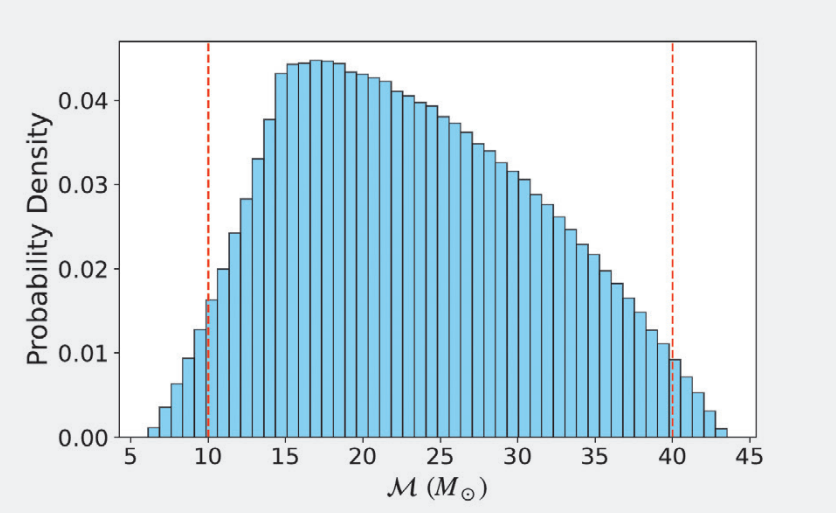

Figure 2: Distribution of the training dataset in terms of the chirp mass ($\mathcal{M}$) of each black hole binary. Dashed red lines mark reference values at 10 and 40 $M_\odot$. Figure from [19].

2.2 The Training Dataset

The AresGW training dataset was built by injecting synthetic waveforms into real noise from the O3a observation period, with an equivalent duration of 35 days, using only coincident data from the aLIGO Hanford (H1) and Livingston (L1) detectors[2]. To avoid unintentional correlations with known O3 detections, the L1 data was randomly time-shifted by up to 240 seconds relative to Hanford. Furthermore, during training, 40% of L1 noise segments were dynamically shuffled to further diversify the input space and reduce overfitting. We note that the data segments used for training were selected based on three criteria: (i) a minimum segment duration of two hours, (ii) high data quality, and (iii) exclusion of 10-second windows around all GWTC-2 events (as detailed in [16]).

Synthetic signals were injected using the IMRPhenomXPHM waveform model [23], which includes precession and higher-order modes. The component masses were sampled uniformly from 7 to 50 $M_\odot$, with spin magnitudes uniformly distributed between 0 and 0.99 and the directions drawn isotropically. Other parameters, including coalescence phase, polarization, inclination, and sky position, were sampled uniformly across their respective domains. Although component masses were sampled uniformly, the resulting chirp mass ($\mathcal{M}$) distribution is skewed due to the nonlinear relationship between $\mathcal{M}$ and the component masses. As shown in Fig. 2, approximately 95% of events fall within the 10–40 $M_\odot$ range, which we consider to be the *effective training range*.

2.3 Methodological Enhancements

The latest version of AresGW incorporates several key enhancements over previous iterations [17, 18], building on the 1-D ResNet backbone to improve classification accuracy and robustness in real detector noise. Those improvements include *double- precision* (FP64) at the softmax output layer and the defi-

2. Real data released for the O3a/b periods can be accessed accessed via the Gravitational Wave Open Science Center (GWOSC) [22].

nition of a *logarithmic ranking statistic*:

$$\mathcal{R}_s = -\log_{10}(1 - \mathcal{R} + 10^{-16}), \qquad (2)$$

where the small offset prevents divergence as $\mathcal{R} \to 1$. Thus, the maximum value of $\mathcal{R}_s$ is capped at 16 due to FP64 precision limits. To further stabilize detection confidence, an ensemble-averaged ranking statistic $\langle \mathcal{R}_s \rangle$ was calculated over 5000 time shifts around a candidate trigger, using a very small step of 0.001 seconds.

Furthermore, in the so-called whitening stage, where the power spectral density is flattened, a 350 Hz low-pass filter was applied (the high-pass filter remained at 15Hz, signifying the rapid loss of sensitivity at lower frequencies, due to environmental noise). This refinement, applied consistently in both training and inference, improves the sensitivity of the network to GW signals otherwise masked by high-frequency noise in the time domain. An example of this improvement is shown in Fig. 3. The top panel shows a short time series, centered around the event GW190511_135545 (with SNR = 7.34 in the Livingston detector). The upper frequency cutoff was set by the Nyquist frequency, i.e. 1024Hz, and the time series appears very noisy. The bottom panel shows the same event, but after applying the 350Hz low-pass filter. One can now distinguish the gravitational waveform more easily, and this also helps the neural network classify such segments as containing real signals.

Another significant improvement is the introduction of a three-tier classification scheme to improve the ranking of real events compared to noise triggers. Those triggers with an initial ranking statistic of $\mathcal{R}_s > 3.5$ are re-evaluated with low-pass filters of 400 Hz and 500 Hz, leading to revised ranking statistics $\mathcal{R}'_s$ and $\mathcal{R}''_s$, respectively. Then, three trigger classes are defined (Default Low-Pass, Selective Noise Rejection and Selective Passband) based on specified empirical criteria that effectively take into account e.g. how noisy the time series is in the vicinity of the real event. These classes are independent and non-exclusive, each characterized by its own false alarm rate (FAR) at various values of the ranking statistic.

Finally, we remove known glitches from the real data, using another deep learning tool, Gravity Spy [24]. This is a CNN-based classifier that effectively classifies loud noise artifacts with SNR > 7.5 into one of several known categories. Any AresGW trigger that came within the duration of a known glitch (including an extra buffer of ±1 second) was excluded, substantially improving the characteristics of the noise background.

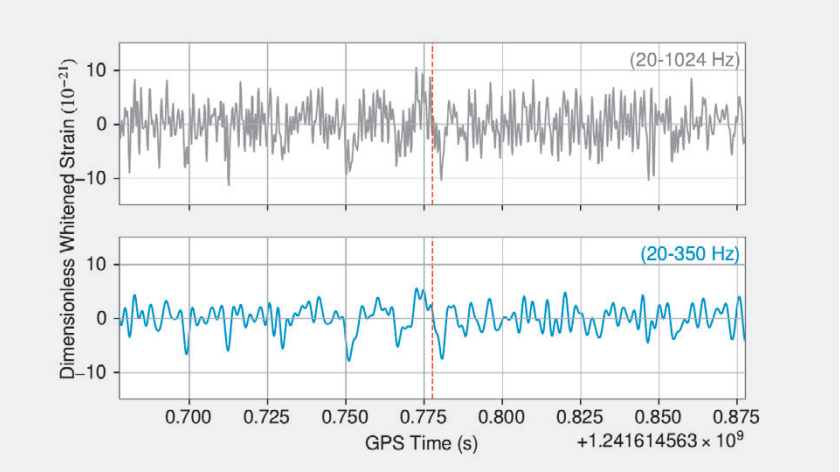

Figure 3: Segment from the Livingston detector showing GW190511_135545. *Top:* 20–1024 Hz band, obscured by high-frequency noise. *Bottom:* 20–350 Hz filter reveals the signal more clearly. The red dashed line indicates merger time. Figure from [19].

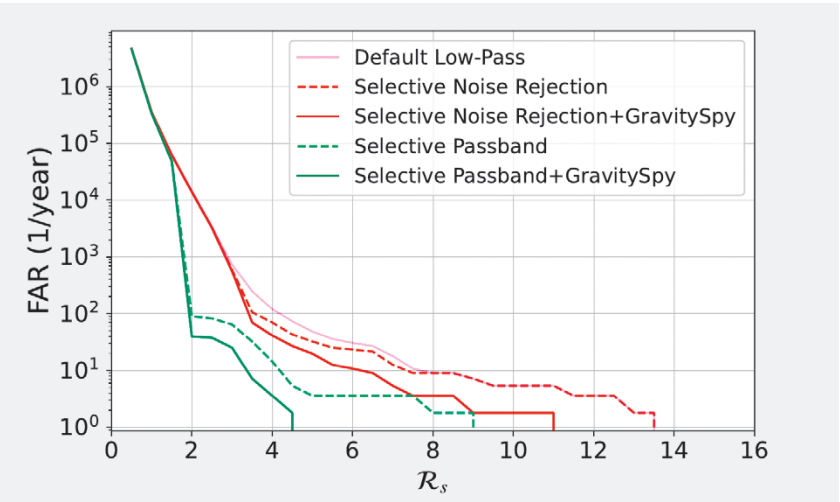

Figure 4: False alarm rate as a function of the ranking statistic $\mathcal{R}_s$ for the O3 dataset. FAR improves significantly when applying trigger classification and glitch removal. Figure from [19].

3. Statistical Analysis of Background and Foreground Triggers

To assess the statistical significance of GW events, it is essential to estimate the background statistics, that is, the rate of false alarms expected from noise alone. This is commonly accomplished by artificially time-shifting data from the two detectors relative to each other, thereby eliminating any true astrophysical coincidences while preserving the noise characteristics. For the analysis of O3 data with AresGW, we constructed a 10-year equivalent time-shifted background. Major GW events and high-SNR glitches (SNR > 7.5) were excluded; however, some residual contamination likely persists, leading to conservative FAR estimates.

Fig. 4 shows the direct calculation of the FAR for the 6.7 months of coincident O3 data (from which known events are excluded) for the three different classes of our trigger classification scheme. It is evident that triggers classified as Selective Passband have significantly fewer false alarms than the other two classes. In addition, removing known glitches using Gravity Spy significantly reduced the FAR even further.

3.1 Astrophysical Probability

The probability that a loud trigger corresponds to a real astrophysical event

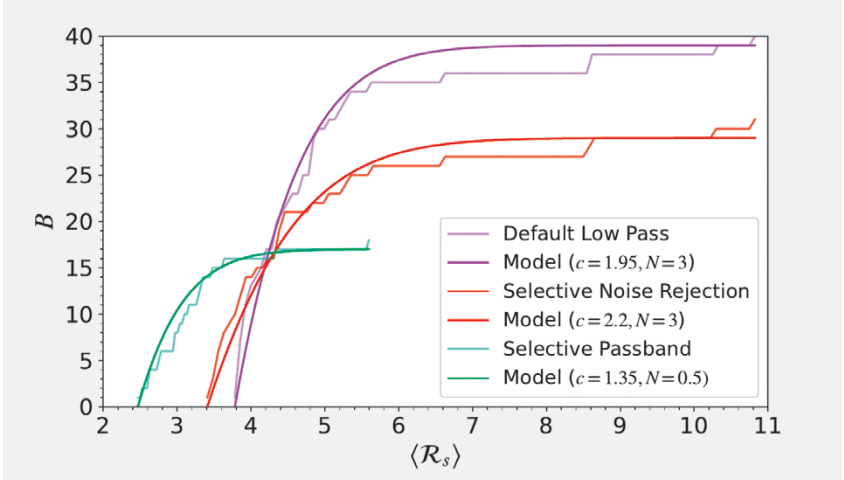

Figure 5: Background distribution of the O3 data, for the different classes of our classification scheme. In all three cases, there is good agreement with our analytical background model of Eq. (7).

can be estimated as follows. First, we calculate the cumulative rate $B(\langle\mathcal{R}_s\rangle)$ of background triggers as an integral of the distribution of triggers from a minimum value to the maximum value found. Then, we calculate the corresponding cumulative rate $F(\langle\mathcal{R}_s\rangle)$ of known real events in the same data. These two cumulative rates can be differentiated, yielding the differential rates:

$$B(\langle\mathcal{R}_s\rangle) = \frac{dB}{d\langle\mathcal{R}_s\rangle}, \tag{3}$$

$$f(\langle\mathcal{R}_s\rangle) = \frac{dF}{d\langle\mathcal{R}_s\rangle}. \tag{4}$$

As a final step, the probability that a given candidate originates from an astrophysical source is quantified by the expression:

$$p_{\text{astro}} = \frac{f(\langle\mathcal{R}_s\rangle)}{f(\langle\mathcal{R}_s\rangle) + b(\langle\mathcal{R}_s\rangle)}. \tag{5}$$

Due to the limited duration of the actual O3 dataset, we smooth out statistical flucuations by adopting analytical models for the cumulative rates $B(\langle\mathcal{R}_s\rangle)$ and $F(\langle\mathcal{R}_s\rangle)$. We calculate the cumulative foreground rate $F(\langle\mathcal{R}_s\rangle)$ using a large number of injections of simulated signals into O3 noise and found that it agrees with a power- law of the form:

$$F(x) = a(x - x_{\text{min}})^b, \tag{6}$$

where $x = \mathcal{R}_s$, with parameters a and b different for each trigger class. Notably, the same exponents extracted for the $F(\mathcal{R}s)$ distribution for the simulated signals led to accurate fits of $F(\langle\mathcal{R}_s\rangle)$ for the actual O3 signals, for all three classes, validating our approach.

For the background, we use the functional form:

$$\hat{B}(x) = \frac{\left(1+\text{erf}\left(\frac{x}{\sqrt{2}}\right)\right)^N - \left(1+\text{erf}\left(\frac{x_{\text{min}}}{\sqrt{2}}\right)\right)^N}{2^N - \left(1+\text{erf}\left(\frac{x_{\text{min}}}{\sqrt{2}}\right)\right)^N} \tag{7}$$

where $B(x)$ is normalized as = B/R_b, with R_b denoting the total number of background events, N is a parameter and x_{min} defines the minimum threshold for valid triggers. For O3 data, we use $x = \mathcal{R}_s/c$ where c is a scaling constant. Fig. 5 shows the actual cumulative background distribution of the O3 data, as obtained with AresGW, and the corresponding analytical fits.

4. Parameter Estimation and Consistency Tests of Candidate Events

The estimation of parameters for candidate GW events was carried out using the Bayesian inference library Bilby [25], assuming uniform priors on detector-frame component masses between $4M_\odot$ and $150M_\odot$. $\mathcal{M}$ and mass ratio q were sampled accordingly, and the redshift–luminosity distance relation was based on Planck15 cosmology [26]. When the posterior distributions approached the edges of the prior range, the relevant bounds were expanded to ensure proper coverage.

Inference was performed using the **dynesty** nested sampler [27], chosen for its efficiency in navigating high-dimensional multimodal likelihood surfaces. All final runs used the IMRPhenomXPHM waveform model [23], which was also used during AresGW training. The posterior results were checked for consistency with the Gaussian likelihood assumption in Bilby.

In parallel, consistency tests were performed using **PyCBC** [28]. These included enforcing inter-detector timing constraints (maximum delay of 10 ms with a 5 ms buffer) and applying a χ^2 veto to test for non-Gaussianity of the residual, when a signal template is subtracted from the data. Events that failed these checks were flagged as likely glitches.

Furthermore, a reweighted SNR ($\hat{\rho}$) was computed for candidate signals, downgrading it to account for the presence of non-Gaussian residuals. The reweighted SNR was computed separately for each LIGO detector and then combined to yield a network-level statistic as well.

5. AresGW Performance on Known GW Events

To assess its performance, AresGW was applied to previously reported GW events and compared against the results of the GWTC [1, 2, 4, 29], OGC [5–8], and IAS [9–11] catalogs. Note, however, that since AresGW was trained exclusively on LIGO data, this evaluation was restricted to periods when both LIGO detectors were operational.

The GWTC catalogs, which are constructed using multiple independent pipelines, include high-confidence detections, each with at least one pipeline assigning a probability $p_{\text{astro}} > 0.5$. These detections are based on matched filtering pipelines such as **pycbc**, as well as unmodeled burst searches such as **cWB**. The OGC catalogs validated known events and contributed additional candidates using matched filtering, while the IAS catalogs focused on signals in the mass-gap regime, also leveraging matched-filter techniques.

5.1 Performance on known O3 events

AresGW was initially evaluated on the set of 43 GW events from the GWTC, OGC, and IAS catalogs that have chirp mass within its effective training range. It detected 34 events, the vast majority with very high confidence and with astrophysical probability consistent with published results. Adding the eight new events found by AresGW (see below) brings the total number of events de-

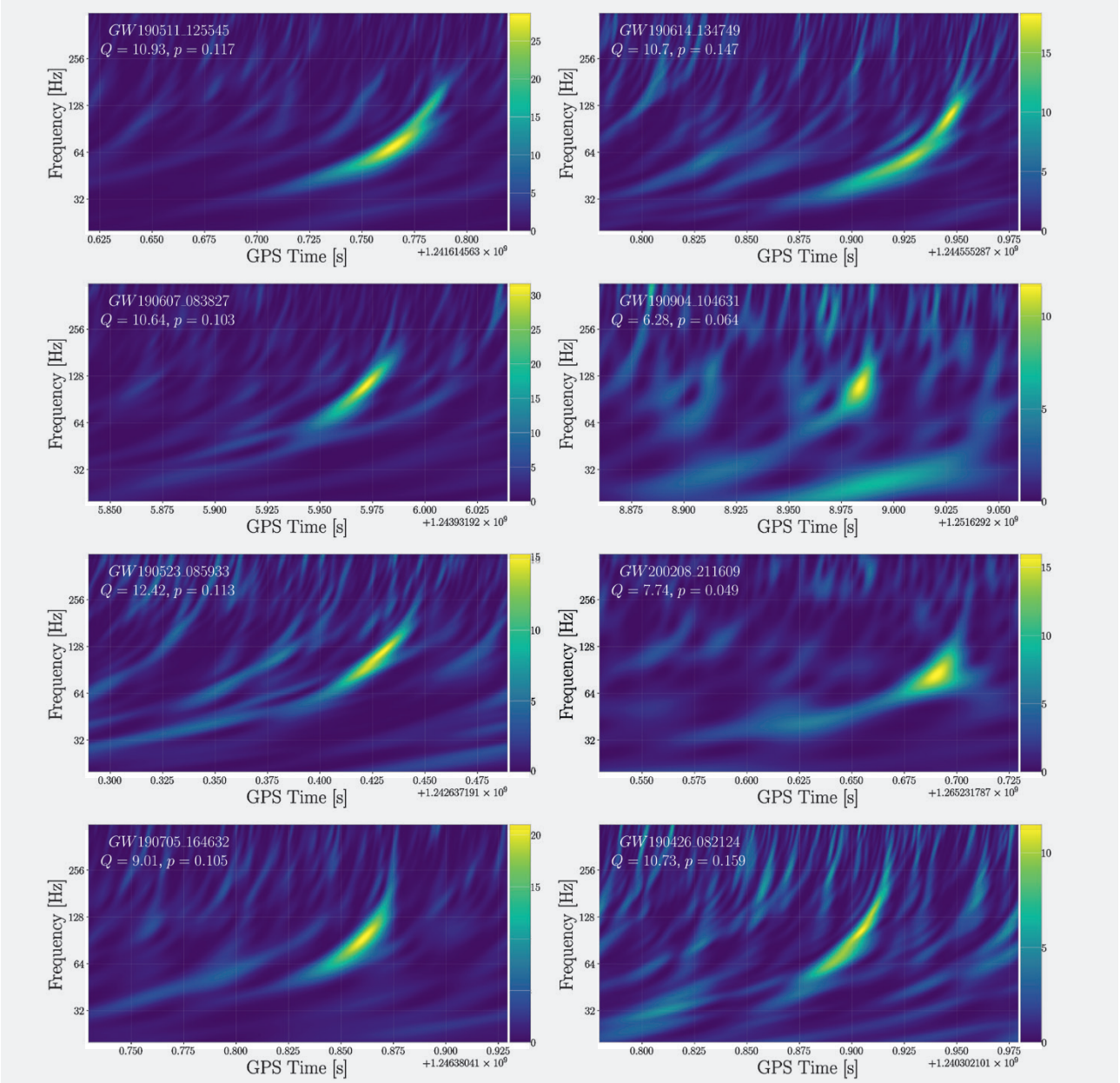

Figure 6: Spectrograms of the eight new gravitational wave detections found with AresGW.

tected by AresGW to 42.[3] Notably, AresGW also identified 10 events that fall outside its effective training range, with high confidence, highlighting its generalization capability. This performance suggests that expanding training to cover a larger range of masses will allow the detection of even more signals.

Overall, AresGW shows exceptional sensitivity within its effective training range, identifying both known and new events with high confidence. This likely reflects its training strategy, which uses simultaneous data from both LIGO detectors to compute a unified ranking statistic, naturally incorporating detector coincidence, unlike other pipelines that initially apply independent thresholds per detector and then check for coincidence between the two detectors.

5.2 Generalization to Virgo and O1 & O2 data

To evaluate AresGW's ability to generalize to different noise environments, we also analyzed data from the Virgo detector in combination with either H1 or L1. Of the eight O3 events listed in GWTC that involved Virgo, four were assigned a high-ranking statistic ($\langle \mathcal{R}_s \rangle \geq 5.6$), indicating promising sensitivity. We also tested AresGW on data from earlier O1 and O2 observing runs. The model correctly identified five out of six O2 events in its effective training range and recovered GW150914 from O1, almost all with the highest possible $\langle \mathcal{R}_s \rangle$ = 16. FAR and p_{astro} estimates for these cases will be the focus of future work.

A key reason behind this robustness is likely AresGW's use of whitening and DAIN, which allow it to effectively process data with varying noise characteristics, such as those from Virgo or earlier LIGO runs, without requiring retraining. These results support the potential of the algorithm for a wider application in multiple observing runs, including the ongoing O4 period, where the detector sensitivity has improved further.

3. The highest number of detections for other, non-optimized, single pipelines in this mass range was 37.

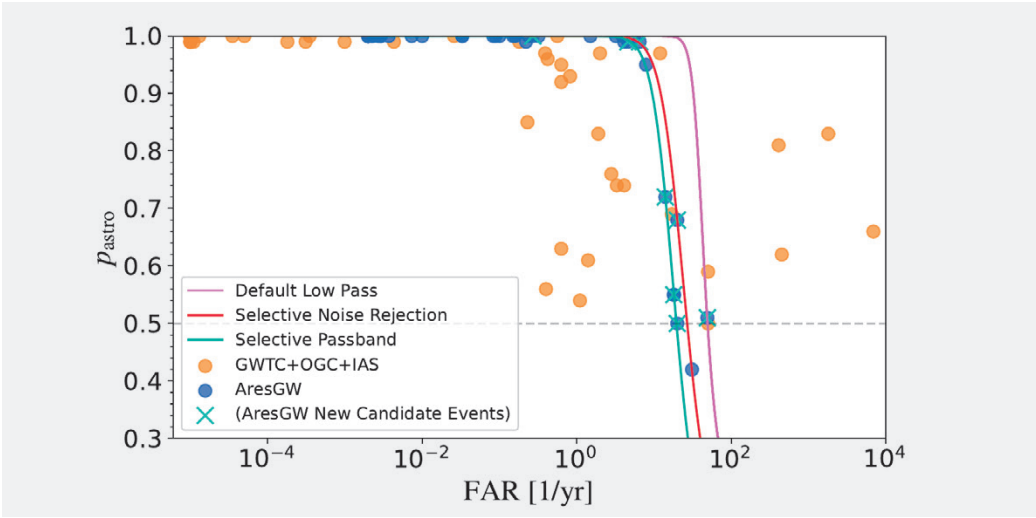

Figure 7: Astrophysical probability vs. false alarm rate. AresGW results are shown in blue, while those from other pipelines are shown in orange. Newly detected events with AresGW are marked with '×'. Figure adapted from [19].

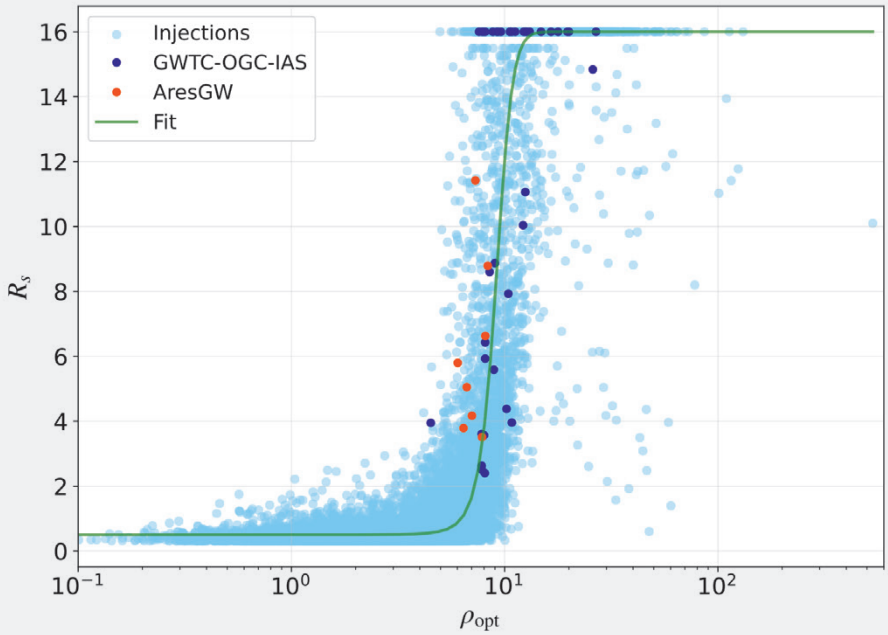

Figure 8: Ranking statistic vs. optimal network SNR for injections (light blue), known events (dark blue), and new AresGW candidates (red). The green curve is a sigmoid fit to the injection data. Figure from [19].

6. New Gravitational-Wave Candidates Discovered by AresGW

In addition to recovering previous published GW signals, AresGW also discovered eight new candidate events with astrophysical probability $p_{\text{astro}} \geq 0.5$. To further assess the credibility of these detections, we analyze their astrophysical significance and inferred source properties. We note that all of our eight new GW detections were subsequently verified by an independent parameter estimation study; see [30].

6.1 Establishing detection confidence

The false alarm rate for each detection was derived using analytical fits specific to each classification category. In particular, candidates in the Selective Passband category achieved significantly lower FARs, between one and two orders of magnitude lower compared to the default class, highlighting the effectiveness of our classification scheme in distinguishing real signals from noise.

The Qp-transform [31] spectrograms shown in Fig. 6 reveal that the newly identified candidates display the expected chirp-like features typical of compact binary coalescence signals. In the absence of hierarchical classification, reviewing these signals would have required a manual inspection of several hundred triggers. However, the combination of the classification scheme and glitch filtering significantly reduced this workload: only 22 noise triggers in the Selective Passband category were misclassified as events, while the Selective Noise Rejection and Default Low-Pass categories contained 39 and 76 such false positives, respectively[4].

Fig. 7 illustrates the relationship between p_{astro} and FAR for all events. AresGW results are shown in blue, while those from other pipelines are shown in orange. As is evident, the values obtained by AresGW fall within the overall range of previously published results. Fig. 8 illustrates the relationship between $\mathcal{R}_s$ and the network SNR across three categories: simulated injections (light blue circles), previously published detections (dark blue circles) and newly identified detections (red circles).

The general trend observed for the injections is described well by a sigmoid-

4. Trigger counts are reported after applying glitch suppression.

Table 1 Parameter estimation for new AresGW detections.

#	Event Name	GPS Time	$\mathcal{M}$ ($M_\odot$)	q	m_1 ($M_\odot$)	m_2 ($M_\odot$)	D_L (Mpc)	χ_{eff}	SNR (H1)	SNR (L1)	SNR $\hat{\rho}$ (network)
1	GW190511 125545	1241614563.77	$28.95^{+9.45}_{-6.86}$	$0.72^{+0.25}_{-0.36}$	$40.7^{+16.2}_{-10.5}$	$28.2^{+11.6}_{-11.2}$	3707^{+3471}_{-2173}	$0.23^{+0.25}_{-0.29}$	2.29	7.34	7.29
2	GW190614 134749	1244555287.93	$25.97^{+16.59}_{-6.20}$	$0.70^{+0.27}_{-0.36}$	$37.0^{+31.8}_{-10.7}$	$25.2^{+15.2}_{-9.7}$	6551^{+9562}_{-3558}	$0.05^{+0.34}_{-0.34}$	3.51	6.08	7.02
3	GW190607 083827	1243931925.99	$30.48^{+7.21}_{-4.68}$	$0.78^{+0.19}_{-0.29}$	$40.5^{+12.0}_{-7.6}$	$31.0^{+9.1}_{-8.2}$	4928^{+2725}_{-2435}	$0.01^{+0.26}_{-0.30}$	4.04	7.29	8.33
4	GW190904 104631	1251629209.01	$21.24^{+5.76}_{-4.40}$	$0.64^{+0.31}_{-0.33}$	$31.3^{+14.5}_{-8.5}$	$19.7^{+7.1}_{-7.2}$	5614^{+4441}_{-2864}	$0.05^{+0.30}_{-0.37}$	4.50	4.88	6.64
5	GW190523 085933	1242637191.44	$23.82^{+10.24}_{-7.95}$	$0.49^{+0.45}_{-0.32}$	$41.7^{+19.3}_{-15.5}$	$19.4^{+14.6}_{-10.5}$	6091^{+6613}_{-3702}	$0.42^{+0.31}_{-0.45}$	3.48	5.14	6.02
6	GW200208 211609	1265231787.68	$18.83^{+4.68}_{-3.18}$	$0.69^{+0.28}_{-0.40}$	$26.9^{+14.6}_{-6.3}$	$18.0^{+6.4}_{-6.9}$	3669^{+3413}_{-1985}	$0.01^{+0.37}_{-0.37}$	4.75	6.22	7.83
7	GW190705 164632	1246380410.88	$27.21^{+7.34}_{-5.24}$	$0.52^{+0.41}_{-0.32}$	$44.7^{+24.8}_{-12.8}$	$23.0^{+11.7}_{-9.8}$	5692^{+4030}_{-2863}	$0.29^{+0.26}_{-0.34}$	4.42	6.88	8.11
8	GW190426 082124	1240302101.93	$17.93^{+4.12}_{-3.42}$	$0.45^{+0.45}_{-0.28}$	$31.5^{+22.5}_{-11.3}$	$13.8^{+6.9}_{-5.2}$	3213^{+4555}_{-1573}	$-0.01^{+0.39}_{-0.50}$	5.15	4.46	6.41

like function, and the new AresGW detections are within the spread of injections and previously known events.

Finally, Table 1 summarizes key inferred parameters for the eight newly reported events. The chirp mass $\mathcal{M}$, the mass ratio q, the individual masses m_1 and m_2, the luminosity distance D_L and the effective spin χ_{eff} are shown. The reweighted network SNR for all events is in the range 6.2 to 8.3, the chirp mass is in the range 18-20 $M_\odot$, the mass ratio is in the range 0.45-0.78, and the luminosity distance is in the range 3.6-6.5 Gpc. The table includes the 90% confidence intervals.

7. Conclusions and Outlook

AresGW, a ResNet-based deep learning algorithm developed at the Aristotle University of Thessaloniki, has demonstrated a transformative potential in advancing gravitational wave astronomy by achieving the first machine learning-based coincident detections of eight new binary black hole mergers in LIGO O3 data, paving the way for more efficient and sensitive GW searches.

The latest version, AresGW model 2, incorporates several advancements: a larger training dataset, double-precision computation, a 350 Hz low-pass filter for both training and inference, glitch removal using Gravity Spy, and a refined ranking statistic. In addition, new frequency and noise filters group triggers into three classes — Default Low-pass, Selective Noise Rejection, and Selective Passband. The latter two apply tailored filtering strategies, with Selective Passband including high- frequency cut-offs (400–500 Hz), resulting in false alarm reductions of at least 70% and 90%, respectively, compared to the default setup.

Trained on BBH mergers within O3a LIGO data (m_1, $m_2 \in (7M_\odot, 50M_\odot)$, $\mathcal{M} \in (10M_\odot, 40M_\odot)$), AresGW model 2 successfully identified 34 of 43 known signals within range. Missed detections corresponded to events with low astrophysical probabilities ($p_{\text{astro}} \leq 0.63$) in the original catalogs. Beyond its training range, it recovered 10 high-confidence events ($p_{\text{astro}} \geq 0.99$), demonstrating strong generalization. The model also found 8 new BBH events, bringing its total in-range detections to 42, making it the most effective pipeline for this parameter range.

Moreover, AresGW model 2 performed effectively on Virgo data combined with one LIGO detector, without retraining. Similarly, on the O1 and O2 data, it validated all but one known event within its effective training range without additional tuning. Operationally, AresGW model 2 runs with high efficiency, analyzing a month of data in under 150 minutes on an NVIDIA RTX A6000; nearly 300 times faster than real time, positioning it well for future low-latency alert systems. Looking ahead, planned enhancements include adapting to different detector configurations, improving glitch rejection, and extending the model to additional astrophysical sources like neutron star mergers, supporting broader multimessenger efforts in upcoming observation runs.

Acknowledgements

We sincerely appreciate the contributions of our collaborators, Panagiotis Iosif, Evdokia C. Koursoumpa, Paraskevi Nousi, Paraskevas Lampropoulos, Nikolaos Passalis, and Anastasios Tefas, whose efforts were instrumental in the research summarized in this review. This research has made use of data or software obtained from the Gravitational Wave Open Science Center (gwosc.org), a service of the LIGO Scientific Collaboration, the Virgo Collaboration, and KAGRA.

References

1. B. P. Abbott et al. GWTC-1: A gravitational-wave transient catalog of compact binary mergers observed by ligo and virgo during the first and second observing runs. *Phys. Rev. X*, 9:031040, Sep 2019.
2. R. Abbott et al. GWTC-2: Compact Binary Coalescences Observed by LIGO and Virgo During the First Half of the Third Observing Run. *Phys. Rev. X*, 11:021053, Jun 2021.
3. R. Abbott et al. GWTC-2.1: Deep extended catalog of compact binary coalescences observed by LIGO and Virgo during the first half of the third observing run. *Phys. Rev. D*, 109(2):022001, 2024.
4. R. Abbott et al. GWTC-3: Compact Binary Coalescences Observed by LIGO and Virgo during the Second Part of the Third Observing Run. *Phys. Rev. X*, 13(4):041039, 2023.
5. Alexander H. Nitz, Collin Capano, Alex B. Nielsen, Steven Reyes, Rebecca White, Duncan A. Brown, and Badri Krishnan. 1-OGC: The First Open Gravitational-wave Catalog of Binary Mergers from Analysis of Public Advanced LIGO Data. *Astrophys. J.*, 872(2):195, February 2019.
6. Alexander H. Nitz, Thomas Dent, Gareth S. Davies, Sumit Kumar, Collin D. Capano, Ian Harry, Simone Mozzon, Laura Nuttall, Andrew Lundgren, and Márton Tápai. 2-OGC: Open Gravitational-wave Catalog of Binary Mergers from Analysis of Public Advanced LIGO and Virgo Data. *Astrophys. J.*, 891(2):123, March 2020.
7. Alexander H. Nitz, Collin D. Capano, Sumit Kumar, Yi-Fan Wang, Shilpa Kastha, Marlin Schäfer, Rahul Dhurkunde, and Miriam Cabero. 3-OGC: Catalog of Gravitational Waves from Compact-binary Mergers. *Astrophys. J.*, 922(1):76, November 2021.
8. Alexander H. Nitz, Sumit Kumar, Yi-Fan Wang, Shilpa Kastha, Shichao Wu, Marlin Schäfer, Rahul Dhurkunde, and Collin D. Capano. 4-OGC: Catalog of Gravitational Waves from Compact Binary Mergers. *Astrophys. J.*, 946(2):59, April 2023.
9. Seth Olsen, Tejaswi Venumadhav, Jonathan Mushkin, Javier Roulet, Barak Zackay, and Matias Zaldarriaga. New binary black hole mergers in the LIGO-Virgo O3a data. *Phys. Rev. D*, 106(4):043009, August 2022.
10. Ajit Kumar Mehta, Seth Olsen, Digvijay Wadekar, Javier Roulet, Tejaswi Venumadhav, Jonathan Mushkin, Barak Zackay, and Matias Zaldarriaga. New binary black hole mergers in the LIGO-Virgo O3b data. *arXiv e-prints*, page arXiv:2311.06061, November 2023.
11. Digvijay Wadekar, Javier Roulet, Tejaswi Venumadhav, Ajit Kumar Mehta, Barak Zackay, Jonathan Mushkin, Seth Olsen, and Matias Zaldarriaga. New black hole mergers in the LIGO- Virgo O3 data from a gravitational wave search including higher-order harmonics. *arXiv e-prints*, page arXiv:2312.06631, December 2023.
12. Elena Cuoco et al. Enhancing gravitational-wave science with machine learning. *Machine Learning: Science and Technology*, 2(1):011002, dec 2020.
13. Vincenzo Benedetto, Francesco Gissi, Gioele Ciaparrone, and Luigi Troiano. Ai in gravitational wave analysis, an overview. *Applied Sciences*, 13(17), 2023.
14. Tianyu Zhao, Ruijun Shi, Yue Zhou, Zhoujian Cao, and Zhixiang Ren. Dawning of a New Era in Gravitational Wave Data Analysis: Unveiling Cosmic Mysteries via Artificial Intelligence – A Systematic Review. *arXiv e-prints*, page arXiv:2311.15585, November 2023.
15. Elena Cuoco, Marco Cavaglià, Ik Siong Heng, David Keitel, and Christopher Messenger. Applications of machine learning in gravitational-wave research with current interferometric detectors. *Living Rev. Rel.*, 28(1):2, 2025.
16. Schäfer et al. First machine learning gravitational-wave search mock data challenge. *Phys. Rev. D*, 107(2):023021, January 2023.
17. Paraskevi Nousi, Alexandra E. Koloniari, Nikolaos Passalis, Panagiotis Iosif, Nikolaos Stergioulas, and Anastasios Tefas. Deep residual networks for gravitational wave detection. *Phys. Rev. D*, 108(2):024022, July 2023.
18. *AResGW* code, 2022. https://github.com/vivinousi/gw-detection-deep-learning.
19. Alexandra E Koloniari, Evdokia C Koursoumpa, Paraskevi Nousi, Paraskevas Lampropoulos, Nikolaos Passalis, Anastasios Tefas, and Nikolaos Stergioulas. New gravitational wave discoveries enabled by machine learning. *Machine Learning: Science and Technology*, 6(1):015054, feb 2025.
20. Kaiming He, Xiangyu Zhang, Shaoqing Ren, and Jian Sun. Deep residual learning for image recognition. In *Proceedings of the IEEE conference on computer vision and pattern recognition*, pages 770–778, 2016.
21. Nikolaos Passalis, Anastasios Tefas, Juho Kanniainen, Moncef Gabbouj, and Alexandros Iosifidis. Deep adaptive input normalization for price forecasting using limit order book data. *IEEE Transactions on Neural Networks and Learning Systems*, 2019.
22. R. Abbott et al. Open Data from the Third Observing Run of LIGO, Virgo, KAGRA, and GEO. *Astrophys. J. Suppl.*, 267(2):29, 2023.
23. Geraint Pratten et al. Computationally efficient models for the dominant and subdominant harmonic modes of precessing binary black holes. *Phys. Rev. D*, 103:104056, May 2021.
24. Michael Zevin and Gravity Spy. Gravity Spy - Integrating LIGO detector characterization, citizen science, and machine learning. In *American Astronomical Society Meeting Abstracts #228*, volume 228 of *American Astronomical Society Meeting Abstracts*, page 109.02, June 2016.
25. Gregory Ashton et al. BILBY: A User-friendly Bayesian Inference Library for Gravitational- wave Astronomy. *ApJS*, 241(2):27, April 2019.
26. Planck Collaboration. Planck 2015 results. XIII. Cosmological parameters. *Astron. Astrophys.*, 594:A13, September 2016.
27. Joshua S. Speagle. DYNESTY: a dynamic nested sampling package for estimating Bayesian posteriors and evidences. *MNRAS*, 493(3):3132–3158, April 2020.
28. Samantha A Usman et al. The PyCBC search for gravitational waves from compact binary coalescence. *Classical and Quantum Gravity*, 33(21):215004, 2016.
29. LIGO Scientific Collaboration and Virgo Collaboration. GWTC-2.1: Deep extended catalog of compact binary coalescences observed by LIGO and Virgo during the first half of the third observing run - parameter estimation data release (version v2), 2022.
30. Daniel Williams. Beyond GWTC-3: Analysing and verifying new gravitational-wave events from community catalogues. *arXiv e-prints*, page arXiv:2401.08709, January 2024.
31. Andrea Virtuoso and Edoardo Milotti. Wavelet-based tools to analyze, filter, and reconstruct transient gravitational-wave signals. *Phys. Rev. D*, 109(10):102010, May 2024.

Exploring the extreme Universe: the TeV window and CTAO

by **Matteo Cerruti**

Université Paris Cité, CNRS, Astroparticule et Cosmologie

1. Looking at the Sky with Cherenkov Light

Gamma-ray astronomy offers a unique window into the non-thermal Universe, populated by a variety of exotic objects often inaccessible to classical optical observations. At the highest energies, we uncover a world of black holes, neutron stars, relativistic jets, and shock waves. Beyond the thrill of discovery, the pleasure of seeing new objects and phenomena for the first time, this field also allows us to test the laws of physics at energies that cannot be probed on Earth. There is a real possibility that this window onto the Universe could help us break the Standard Model, our current framework for fundamental physics, and guide us toward the next one.

"Gamma-ray" is a general term for photons with energies greater than those of X-rays (E > 100 keV). What began as "classical" gamma-ray astronomy has now extended over nine orders of magnitude in energy. We speak of high-energy gamma rays (100 MeV to 100 GeV, GeV astronomy), very-high-energy gamma rays (100 GeV to 100 TeV, TeV astronomy), and ultra-high-energy gamma rays (above 100 TeV — PeV astronomy). The difference in energy between a 1 MeV and a 1 PeV gamma-ray is the same as between an X-ray photon and a GHz radio wave, showing by how much we expanded the available observing window. While MeV and GeV gamma rays are best observed from space, the most efficient way to study energies above 10 GeV is from the ground—using the Earth's atmosphere as a detector. When a gamma-ray photon interacts with air molecules, it initiates a particle cascade (electron-positron pairs), which can travel faster than the speed of light in air (v > c/n), emitting Cherenkov radiation. TeV observatories are essentially large optical telescopes that image this Cherenkov light.

This indirect observing technique has a major advantage: the effective area is defined by the portion of atmosphere seen by the telescopes, which, with current instrumentation, is of the order of 0.1 square kilometers — orders of magnitude larger than the collecting area of space-based detectors. There are however several challenges. First, Cherenkov flashes are extremely faint and last only few nanoseconds. Cherenkov telescopes therefore require large mirrors to collect enough light, ultra-sensitive cameras capable of detecting single photons, and fast electronics to trigger on such short-lived signals. The second challenge comes from Nature itself: not only gamma rays, but also the much more abundant cosmic rays (mainly protons, light nuclei, and electrons) can trigger air showers that produce Cherenkov light. Fortunately, hadronic cascades have a more irregular and broader structure than electromagnetic ones, and we can thus develop algorithms to efficiently compute the probability that a given image is 'gamma-like'. Finally, the detector—the atmosphere—is not under our control, and its properties are not perfectly known. To infer the properties of the incoming gamma ray from the observed cascade, we rely heavily on computationally intensive Monte Carlo simulations, modeling the atmospheric conditions and the cascade developments as accurately as possible.

Despite the observational constraints — operation is limited to clear, moonless nights, and the field of view is relatively narrow — the technique is remarkably powerful. Running instruments achieve angular resolution at the arcminute scale, energy resolution of 15–20%, and sensitivities sufficient to detect sources as faint as 1% of the Crab Nebula's flux in about 50 hours of exposure. For strong flares, detections can be made within minutes.

Figure 1: Artistic rendering of Cherenkov flashes observed by CTAO telescopes. Credit: CTAO

2. From Pioneering Flashes to a Flourishing Field

The Cherenkov technique is now almost 75 years old, and we are currently in its third generation of instruments. The first milestone came in 1953 with the successful detection of Cherenkov light from cosmic-ray showers [1]. The second generation of telescopes, such as HEGRA, CAT, and Whipple, marked significant progress, thanks mainly to the introduction of more pixels in the camera to better reconstruct the properties of the cascade, and to the combination of multiple telescopes for stereoscopic imaging of the cascades. TeV astronomy was truly born in 1989, when the Whipple 10-meter telescope detected its first TeV source: the Crab pulsar wind nebula [2]. In these early years, the number of known sources remained small. The

field was new, and each detection was a groundbreaking discovery. Among the early milestones were the first detections of extragalactic sources — Mrk 421 and Mrk 501 — establishing blazars as TeV emitters [3, 4].
The field took a major leap forward with the advent of third-generation instruments: H.E.S.S., MAGIC, and VERITAS.

- H.E.S.S. is an array of five Cherenkov telescopes in Namibia. The original four 12-meter telescopes began operations in 2004; a fifth, 28-meter telescope was added in 2012.
- MAGIC consists of two 17-meter telescopes on the Canary island of La Palma, operating in stereoscopic mode since 2009.
- VERITAS is an array of four 12-meter telescopes located in Arizona, at the Whipple Observatory, operational since 2007.

These arrays brought higher sensitivity, better angular resolution, and broader energy coverage compared to their predecessors. Combined with improved data analysis techniques and machine learning algorithms, they revealed a surprisingly rich TeV sky.
Thanks to H.E.S.S., MAGIC, and VERITAS, more than 250 sources have been discovered at TeV energies [5]. In addition to pulsar wind nebulae, we now know that in our Milky Way supernova remnants, pulsars, star clusters, molecular clouds illuminated by cosmic-rays, gamma-ray binaries, micro-quasars, novae, and superbubbles, produce TeV photons. Outside of our galaxy, in addition to blazars we have also detected radio-galaxies, starburst galaxies, and gamma-ray bursts. Remarkably, several of the TeV sources remain unidentified, without a clear counterpart at lower energies. In a little more than 20 years, TeV astronomy has evolved from a niche field to an essential component of high-energy astrophysics, providing complementary insights to lower energy instruments such as X-rays and GeV gamma-ray telescopes, as well as higher energy instruments such as LHAASO that are sensitive up to the PeV band.

3. Recent Highlights: What the TeV Sky Has Taught Us

The last decade has been especially fruitful, with a number of groundbreaking discoveries that demonstrate the scientific impact of TeV observations. The following list is obviously biased due to the space limitation, but it shows some examples of the revolution brought forward by H.E.S.S., MAGIC and VERITAS

The Milky Way and Sgr A*

H.E.S.S. is uniquely placed in the Southern Hemisphere, with a direct view of the central region of the Milky Way. H.E.S.S. observations have revealed that our Galaxy is full of TeV emitters, including the existence of many 'dark' gamma-ray sources, without clear counterparts [6]. Remarkably, there exists a point-like TeV source coincident with Sgr A*, the supermassive black hole at the center of the Milky Way. The TeV emission from Sgr A* appears to be non-variable, and its spectrum reaches tens of TeV without any hint of a cut-off. This could indicate that cosmic rays of PeV energies are accelerated by, or near, the supermassive black hole [7].

Blazars

All instruments have detected intense gamma-ray flares from blazars with variability timescales of just a few minutes [8,9,10]. From simple causality arguments ($R/c < t$), this implies emitting regions smaller than the size of the event horizon of the central black hole — unless the emitting region in the jet is moving with extremely high Lorentz factors ($\Gamma \sim 50$ or more). In addition, very-high-energy photons have been observed from Flat-Spectrum Radio Quasars, blazars characterized by bright optical/IR photon fields (from the accretion disk, the Broad-Line Region, and the torus), indicating that the emitting region must be located far from the black hole in order to avoid absorption via pair production on those fields [11].

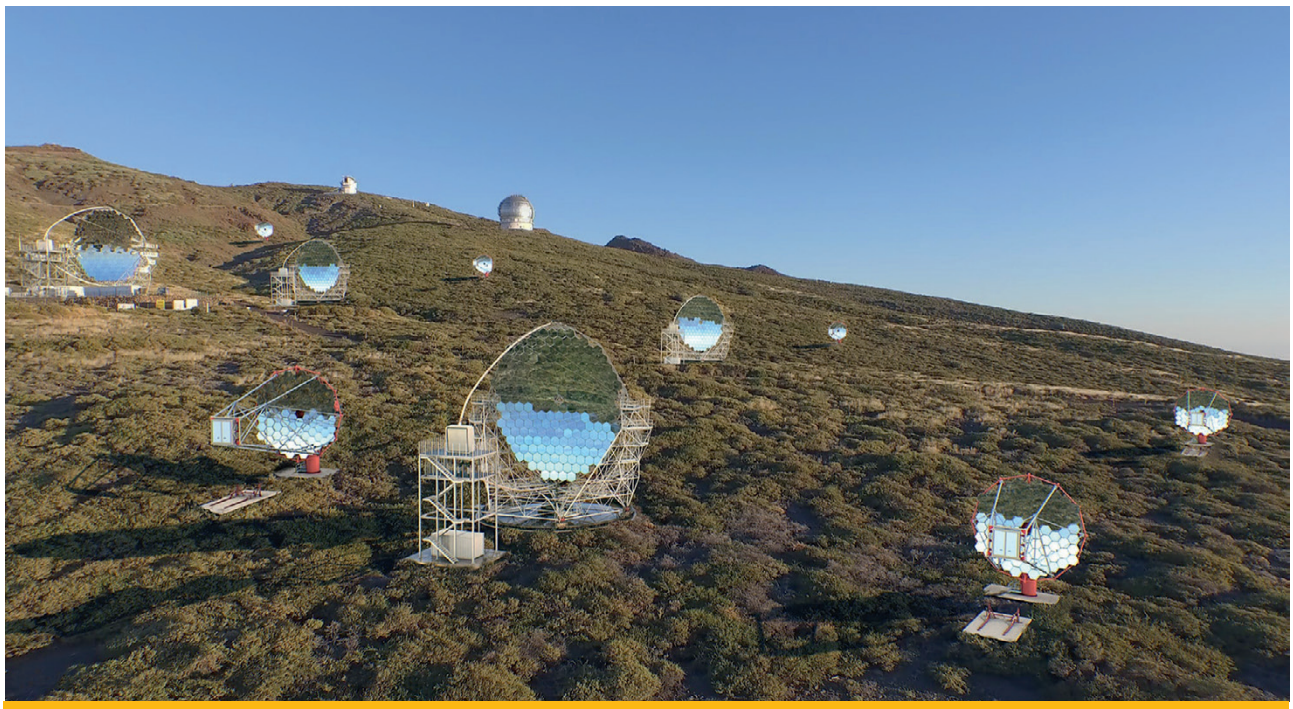

Figure 2: Artistic rendering of CTAO–North with LST-1 on Far Left. Credit: CTAO

Pulsars

Pulsed very-high-energy emission has been observed from several pulsars. MAGIC and VERITAS detected pulsed emission from the Crab pulsar extending beyond 100 GeV, up to nearly 2 TeV [12, 13]. Subsequently, H.E.S.S. discovered a new spectral component in the spectrum of the Vela pulsar, with pulsed emission at several TeV [14], spectrally distinct from the GeV component seen by Fermi-LAT.

Gamma-ray-bursts

Gamma-ray bursts (GRBs) are powerful explosions, originally detected in the low-energy gamma- ray band (hundreds of keV). They are known to produce GeV photons, but for many years it was unclear whether they could reach TeV energies. Their detection with Cherenkov telescopes has been challenging due to the limited field of view of the instruments and the rapidity of these transient events. It required, in addition to continuous improvements in the instrument response to alerts and fast repointing capabilities, a lot of trials — and some luck. The first TeV GRBs were detected by MAGIC and H.E.S.S. a few months apart [15,16]

Neutrino counterparts

In 2017, the IceCube Neutrino Observatory detected a ~290 TeV neutrino coincident in direction and time with the blazar TXS 0506+056. MAGIC and Fermi-LAT confirmed a gamma-ray flare from the source, marking the first multi-messenger identification of a potential cosmic neutrino source [17]. While still below the 5-sigma significance threshold, this event highlighted the power of joint observations across messengers.

4. CTAO: A New Era for Ground-Based Gamma-Ray Astronomy

The future of Cherenkov astronomy is bright, and brings the name of the Cherenkov Telescope Array Observatory (CTAO). Coming from the fusion of the three collaborations that built H.E.S.S., MAGIC, and VERITAS, it is designed to be the worldwide flagship observatory for TeV astronomy in the coming decades. It will offer an order-of-magnitude improvement in sensitivity over current instruments, with wider energy coverage, larger field of view, and better angular resolution [18, 19].

CTAO will be composed of two arrays: CTA-North on the Canary island of La Palma (Spain), close to the MAGIC site, and CTA-South in Paranal (Chile). It will be composed of telescopes of different sizes, to maximize the energy coverage: Large-Sized Telescopes (LSTs) for low energies (20–200 GeV), Medium-Sized Telescopes (MSTs) for the core 100 GeV–10 TeV range, and Small-Sized Telescopes (SSTs) optimized for the highest energies (above 10 TeV). The southern site will host MSTs and SSTs, focusing on the highest energies (although there are discussions ongoing to also add LSTs at the southern site), while CTA-North will feature LSTs and MSTs, focusing on extragalactic sources. The first of the CTA-North telescopes (LST-1) is already taking data, and the four LSTs are expected to be installed by the end of the year. By the beginning of the next decade, CTAO will be fully operational as the most sensitive gamma-ray instrument worldwide. Arguably the biggest change in the TeV community is that CTAO will operate as an open observatory: time will be allocated through a peer-reviewed proposal process, and data will be made public after a proprietary period. Analysis tools and user support will be provided, significantly lowering the barrier to entry for non-experts. The goal is to make TeV data as accessible as optical or X-ray data. Non-experts can already get familiar with Gammapy [20], the official analysis tool and the first open CTAO data challenge is expected for next year.

5. An Invitation to Greek Astronomers

If you study compact objects, transients, star-forming regions, or even cosmology and physics beyond the Standard Model — CTAO has something to offer. Its capabilities span many domains: from probing the mechanisms of particle acceleration and jet propagation, to constraining models of dark matter annihilation. It will bridge observations across the electromagnetic spectrum, and connect with neutrino and gravitational wave detectors.

TeV astronomy has completed its journey from small collaborations trying to catch faint blue flashes in the sky, to a coordinated, global observatory that gives access to the TeV window to everyone in the world. So, whether you are a long-time gamma-ray enthusiast or a newcomer, you can start already by playing with the Gammapy software, attending the CTAO science symposia, and if you are a student, joining one of the upcoming doctoral schools [21]. CTAO is only few years away, to be your gateway to the extreme Universe. Πρὸς τὰ ἄστρα!

References

[1] Galbraith W. and Jelley J. V., Nature, Volume 171, Issue 4347, pp. 349-350 (1953)
[2] Weekes, T. et al., Astrophysical Journal v.342, p.379 (1989)
[3] Punch, M. et al., Nature, Volume 358, Issue 6386, pp. 477-478 (1992)
[4] Quinn, J. et al., Astrophysical Journal Letters v.456, p.L83 (1996)
[5] see the updated TeV catalog, http://www.tevcat.org/
[6] H.E.S.S. Collaboration et al., Astronomy & Astrophysics, Volume 612, id.A1, 61 pp. (2018)
[7] H.E.S.S. Collaboration et al., Nature, Volume 531, Issue 7595, pp. 476-479 (2016)
[8] Aharonian, F., et al., The Astrophysical Journal, Volume 664, Issue 2, pp. L71-L74 (2007)
[9] Aleksic, J., et al., Science, Volume 346, Issue 6213, pp. 1080-1084 (2014)
[10] Arlen, T., et al., The Astrophysical Journal, Volume 762, Issue 2, article id. 92, 13 pp. (2013)
[11] MAGIC Collaboration et al., Science, Volume 320, Issue 5884, pp. 1752- (2008)
[12] Ansoldi, S., et al., Astronomy & Astrophysics, Volume 585, id.A133, 6 pp. (2016)
[13] VERITAS Collaboration et al., Science, Volume 334, Issue 6052, pp. 69- (2011)
[14] H.E.S.S. Collaboration et al., Nature Astronomy, Volume 7, p. 1341-1350 (2023)
[15] Abdalla et al., Nature, Volume 575, Issue 7783, p.464-467 (2019)
[16] MAGIC Collaboration et al., Nature, Volume 575, Issue 7783, p.455-458 (2019)
[17] IceCube Collaboration et al., Science, Volume 361, Issue 6398, id. eaat1378 (2018)
[18] Acharya B.S., Astroparticle Physics, Volume 43, p. 3-18 (2013)
[19] 'Science with the Cherenkov Telescope Array' Edited by CTA Consortium. Published by World Scientific Publishing Co. Pte. Ltd (2019)
[20] Donath, A., et al., Astronomy & Astrophysics, Volume 678, id.A157, 23 pp. (2023)
[21] see https://school.ctao.org/

NELIOTA: The long-term monitoring campaign for lunar impact flashes and meteoroid characterization

by **Alexios Liakos and Alceste Bonanos**

Institute for Astronomy, Astrophysics, Space Applications and Remote Sensing, National Observatory of Athens

Introduction

Lunar impact flashes (LIFs) are produced by relatively large meteoroids, typically in the centimeter-to-decimeter size range. Such objects are considered among the most hazardous due to their kinetic energy and potential to cause observable optical phenomena from Earth. In contrast, the majority of meteors detected in Earth's atmosphere originate from smaller particles; only those that result in bolides or fireballs are comparable in size to the meteoroids responsible for LIFs. However, such high-energy atmospheric events are rarely recorded from a single observational site, given the limited sky coverage (~6×10^4 km^2), necessitating extensive observational networks for adequate monitoring.

Meteors and LIFs involve fundamentally different physical processes. Meteors undergo ablation due to atmospheric friction, enabling analysis of parameters such as entry velocities, orbital origins, and potential meteorite survival. LIFs, on the other hand, occur in the absence of an atmosphere. The Moon, with its vast impact area (~1.9×10^7 km^2 on the near side), provides an ideal natural laboratory for studying the flux and characteristics of larger meteoroids and asteroids. Meteoroids directly impacting the lunar surface have their kinetic energy partitioned into (a) thermal energy that heats the target material, (b) kinetic energy transferred to the ejecta, and (c) mechanical energy for crater excavation. The thermal component leads to the emission of visible light — manifesting as the impact flash.

LIF observations are essential for deriving the size-frequency distribution of meteoroids and have direct implications for spacecraft risk assessment for both satellites and crewed missions and planning for future lunar infrastructure. For these reasons, the European Space Agency (ESA) initiated the Near-Earth objects Lunar Impacts and Optical TrAnsients (NELIOTA) project in 2015 at the National Observatory of Athens, in parallel with other efforts by the NASA Marshall Space Flight Center (Suggs et al. 2014) and the MIDAS project (Madiedo et al. 2015a, 2015b) in Spain. The project initially involved telescope upgrades, software development, and system validation. Lunar monitoring observations commenced in February 2017 and continued through January 2021. In June 2021, the NELIOTA team integrated into ESA's Consolidating Activities Regarding Moon, Earth, and NEOs (CARMEN) initiative, with operations extending through mid-August 2023. The short-term objectives of NELIOTA included the detection of LIFs, estimation of impact temperatures, and derivation of physical properties (mass, size) of the impacting meteoroids. The mid-to-long-term goal was to determine the flux density of these objects in near-Earth space, characterized by size distribution and impact frequency.

Figure 1. The Kryoneri Observatory building (left) and the 1.2 m telescope (right).

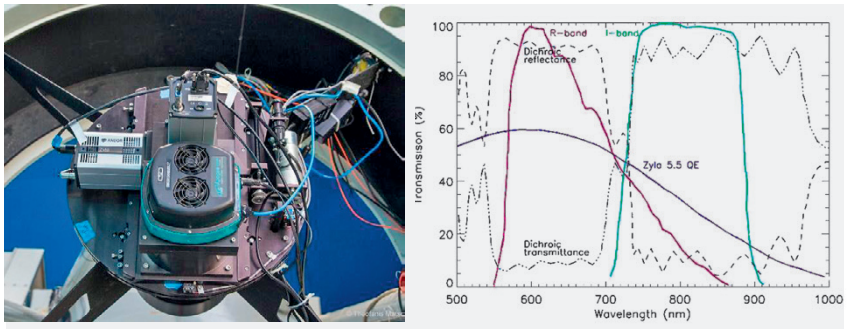

Figure 2. *Left*: The prime focus instrument of the Kryoneri telescope with the two sCMOS ZYLA 5.5 cameras (grey devices) attached on the dichroic beam splitter. The light-green-black device is a CCD camera that is used for other projects. *Right*: The performance of the optical system (dichroic, filters, zyla cameras) of Kryoneri telescope taking into account the Quantum Efficiency (QE; blue solid line) of the cameras, the transmittance of the *R* and *I* filters (red and green solid lines, respectively) and the dichroic (black dashed and dot dashed lines). The dichroic is centered at 730 nm with a throughput greater than 90%. The figure is from Xilouris et al. (2018).

Site, telescope and cameras

NELIOTA operates the largest telescope globally dedicated to the detection of lunar impact flashes — the Kryoneri telescope (Fig. 1), situated on Mt. Kyllini in the Peloponnese at an altitude of 930 m. This instrument is a 1.2 m prime-focus

reflector with an f/3 focal ratio. The lunar monitoring setup employs two identical front-illuminated scientific CMOS (sCMOS) cameras (Andor Zyla 5.5), each offering a resolution of 2560×2160 pixels and a pixel size of 6.48 μm (Fig. 2).

The optical path is divided into two spectral channels — below and above 730 nm — using a dichroic beam splitter. A focal reducer positioned before the dichroic shortens the effective focal length to 3.36 m, yielding an effective focal ratio of f/2.8. This configuration results in a field of view of approximately 17.0 × 14.4 arcmin². Each camera is mounted at the end of one of the split optical paths and is fitted with Johnson-Cousins photometric filters. Specifically, the first camera is equipped with a red (R_c) filter, centered at λ_R = 641 nm, while the second camera uses a near-infrared (I_c) filter, centered at λ_I = 798 nm (Fig. 2).

Observations and data reduction

Observations were conducted during lunar phases between 10% and 45% illumination, targeting the night-side of the Moon's Earth-facing hemisphere. The upper illumination limit was defined by increased background noise due to scattered light from the sunlit portion of the lunar surface. Typically, the Moon was observed on 4 to 8 nights per month, divided into two observing windows before and after the new Moon. Observing sessions ranged from 30 min to approximately 5.5 h, depending on lunar elevation (limited to elevations >10°). Observations commenced 20 min after sunset during the waxing phase and concluded 20 min before sunrise during the waning phase. The NELIOTA setup covered a projected lunar surface area of approximately 3×10⁶ km².

Each observation session was segmented into 15-min intervals ("chunks"). Standard photometric stars were observed before and after each chunk for magnitude calibration of the LIFs. The twin cameras operated simultaneously in the *R* and *I* photometric bands, acquiring data at 30 frames per second in 2×2 binning mode, resulting in a spatial resolution of ~0.8 arcsec per pixel. Each exposure lasted 23 ms and was followed by a 10 ms readout interval. The cameras were synchronized to within 6 ms, with absolute timing accuracy better than 9 ms.

Data acquisition and storage were managed by dedicated software developed for the project, NELIOTA-OBS. This software automated the nightly observation plan, including lunar chunk scheduling, standard star acquisition, and calibration imaging. It also generated metadata for each observation and managed real-time data archiving.

Post-acquisition data were processed using NELIOTA-DET, a custom pipeline for calibration, background subtraction, and impact event detection. The pipeline employed a time-weighted background subtraction algorithm, in which frames preceding a given image contributed to a background model with higher weight given to the most recent frames. The residual image was then scanned for sources exceeding a predefined threshold. When ten or more contiguous pixels surpassed this threshold, the corresponding frame, along with the seven preceding and seven succeeding frames, were archived for further inspection. Frames from both cameras were stored regardless of which channel initially triggered the detection. An additional tool within NELIOTA-DET enabled spatial localization of candidate events through cross-referencing observed lunar features with a high-resolution lunar atlas.

Candidate events were reviewed by an expert analyst who assessed each detection following the validation flowchart established in Liakos et al. (2020). Each event was classified as either (a) validated, (b) suspected, or (c) spurious (e.g., cosmic ray hits, satellite glints). Aperture photometry was applied to all validated and suspected events to derive photon fluxes, which were converted into apparent magnitudes using the calibration data from standard star observations. Due to the heterogeneous lunar background and glare from the illuminated lunar region, standard photometric techniques were not directly applicable. Instead, photometry was performed on background-subtracted "difference images" and optimal aperture settings were selected for both impact flashes and standard stars observed in temporal proximity. Final magnitude estimates for LIFs were calculated using the Pogson relation.

All validated and suspected LIF detections were uploaded within 24 hours to the project's public archive (https://neliota.astro.noa.gr/) via the NELIOTA-ARC software. The data were made openly available for both scientific research and educational outreach. An example of a LIF detection is illustrated in Fig. 3.

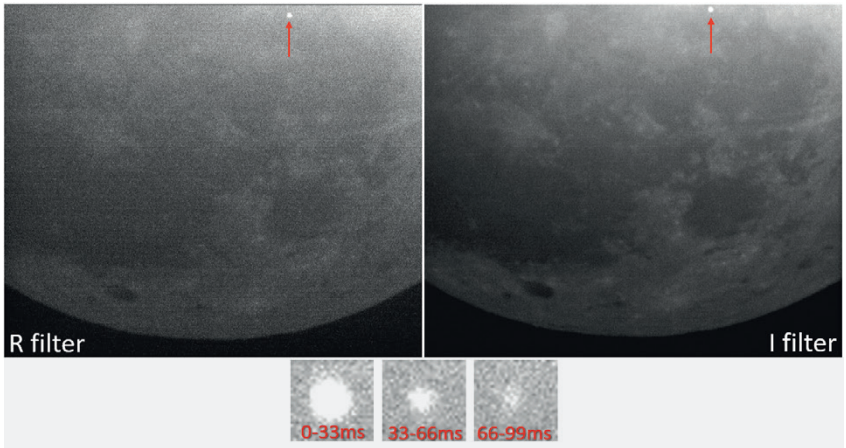

Figure 3. Example of a LIF detection indicated by the red arrow in both cameras by the NELIOTA project. The lower images are successive frames of this specific LIF in the *I* band showing its rapid magnitude decrease.

Methods for determining physical parameters

The NELIOTA project provided the first observational evidence enabling direct temperature estimation of LIFs. By simultaneously measuring the emitted flux in two photometric bands (*R* and *I*), it was possible to derive the temperature of each flash through comparison of intensities in these wavelengths. Assuming black-body radiation, each temperature corresponds to a specific *R*-to-*I* flux ratio. Instrumental fluxes for both the LIF and a nearby standard star were recorded and the known *R* and *I* magnitudes of the standard star were used to convert instrumental values in-

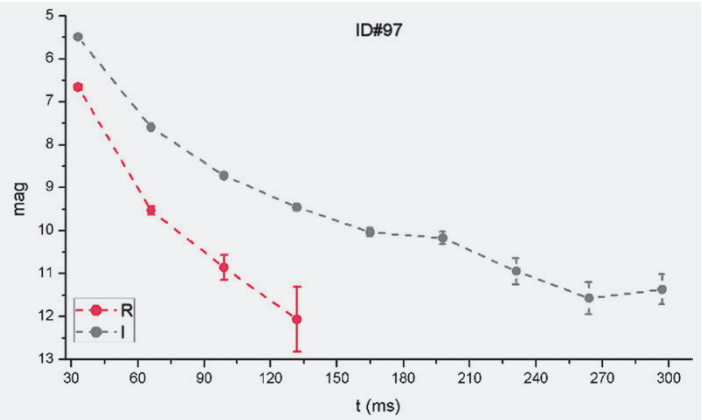

Figure 4. Light curves in *R* and *I* bands of a LIF.

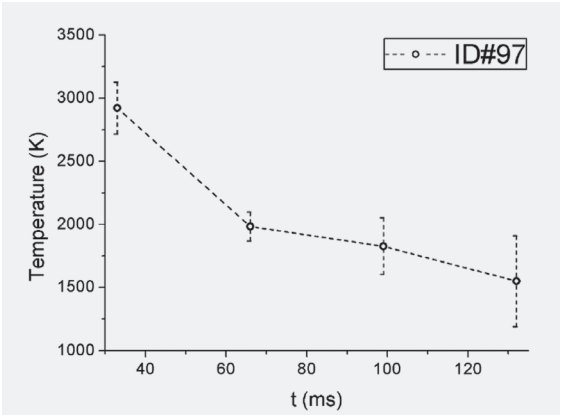

Figure 5. Temperature curve of a multi-frame LIF.

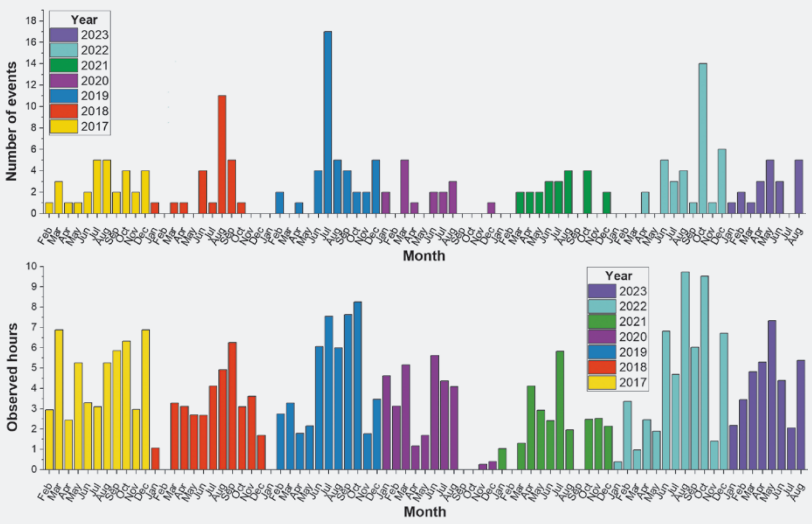

Figure 6.
Statistics of the validated lunar impact flashes (top panel) and the monthly hours of observations (bottom panel) of the NELIOTA campaign between Feb. 2017 and mid-Aug. 2023. During this period, 192 validated flashes were detected within 283.4 hrs of observations.

to calibrated fluxes for the flash. From this, the *R*–*I* flux ratio — or color index — was determined. Applying Planck's black-body radiation law, the temperature of the LIF was then calculated. In cases where the LIF was detected across multiple frames in both bands (Fig. 4), its thermal evolution was also tracked, enabling derivation of cooling curves (Fig. 5). The luminous energy E_{lum} of the flashes was calculated using a widely adopted method (e.g., Suggs et al. 2014; Madiedo et al. 2018), based on the stellar luminosity formula adapted to LIFs. This approach utilizes the observed flux within a defined wavelength interval around a central wavelength and converts it into luminosity following the method of Bessell et al. (1998a,b). The total energy in each band was computed from the apparent magnitudes of the flash, and the kinetic energy of the meteoroid was subsequently derived by assuming a luminous efficiency (η) — the ratio of luminous to kinetic energy — ranging between 5×10^{-4} and 5×10^{-3}, with a typical value of 1.5×10^{-3} (e.g., Bellot Rubio et al. 2000a,b; Ortiz et al. 2006; Moser et al. 2011; Swift et al. 2011; Bouley et al. 2012; Suggs et al. 2014; Madiedo et al. 2015b, 2017, 2018, 2019).

A major source of uncertainty in estimating meteoroid mass is the assumption of both impact velocity and luminous efficiency. For meteoroid streams, impact velocities are well constrained from meteor shower observations. However, for sporadic meteoroids, the velocity can vary significantly — typically between 17 and 24 km s^{-1}. Consequently, associating detected LIFs with known active meteoroid streams significantly reduces this uncertainty, leading to more reliable parameter estimates. To investigate potential associations, the methodology of Ortiz et al. (2015) and Madiedo et al. (2015a,b) was applied. If an impact could be linked to a meteoroid stream, the impact velocity was assigned the corresponding value from literature (e.g., Hughes 1987; Jenniskens 1994; Bellot Rubio et al. 2000; Brown et al. 2002, 2010; Madiedo et al. 2015b). Otherwise, a representative value within the 17–24 km s^{-1} range was used for sporadic events. The meteoroid mass was then computed using the standard kinetic energy equation.

The radius of the impacting meteoroid was estimated from its mass, assuming a bulk density. For meteoroids associated with streams, density values were adopted from Babadzhanov & Kokhirova (2009), who reported average densities for meteoroids from ten major streams, based on their parent bodies. For sporadic meteoroids, a standard bulk density of 1.8 g cm^{-3} was assumed. The meteoroid radius was then calculated using the standard mass–density–volume relationship. Expected crater sizes were subsequently estimated using the scaling law developed by Gault (1974); see also Melosh (1989).

Results

Between February 2017 and mid-August 2023, the NELIOTA campaign recorded a total of 192 validated and 103 suspected LIFs over a cumulative ob-

serving time of 283.4 hours (Fig. 6). The magnitude distributions of these events in both observed bands are presented in Fig. 7. Among the validated LIFs, 65% had durations exceeding 33 ms in the *I* band, allowing the construction of 125 light curves. Furthermore, 30 validated LIFs were detected in multiple frames in both filters, enabling analysis of their thermal evolution.

The spatial distribution of the detected LIFs on the lunar surface is illustrated in Fig. 8. Observations deliberately excluded the polar regions, which consistently include parts of the lunar terminator, leading to image saturation and elevated background levels. Instead, the focus was on the eastern and western hemispheres. Slightly more detections were made in the western hemisphere, a consequence of marginally longer observing times there, attributed to observational chance. This indicates that LIF detection is independent of the hemisphere observed, suggesting that meteoroid impacts are uniformly distributed across the lunar surface. NELIOTA's detection rate for sporadic meteoroids ranges from 0.6 to 0.9 LIFs per hour (based on validated and combined validated/suspected events), while for meteoroid streams, the rate increases to 1–1.9 LIFs per hour. When normalized to the effective lunar surface area observed, these rates correspond to 1.96-2.81 LIF h^{-1} km^{-2} for sporadic impacts and 3.32-6.14 LIF h^{-1} km^{-2} for stream-associated impacts.

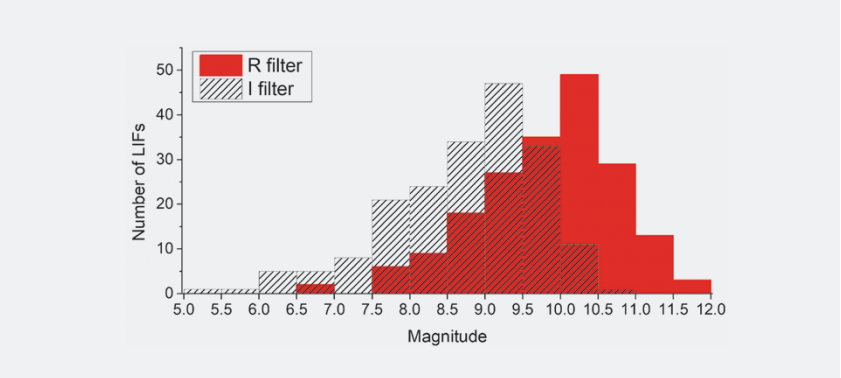

Figure 7. Magnitude distributions of the 192 validated lunar impact flashes in *R* and *I* bands detected throughout the NELIOTA campaign. Our setup, due to the size of the telescope mirror, is able to validate lunar impact flashes up to approx. 12th magnitude in the *R* band.

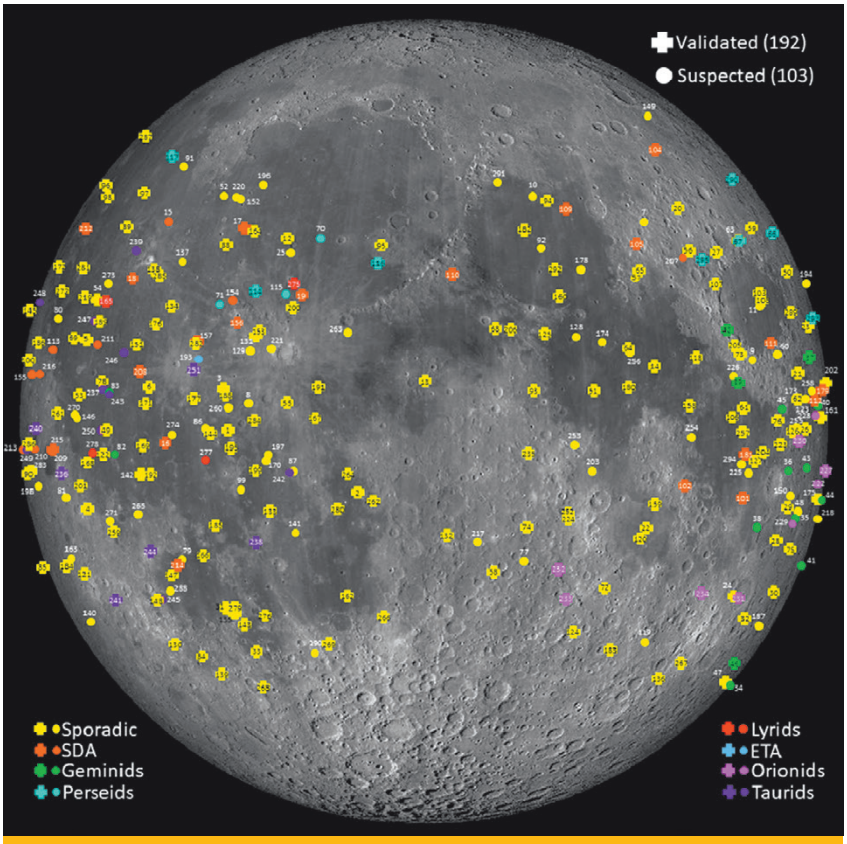

Figure 8. Locations of lunar impact flashes detected by the NELIOTA campaign between 2017-2023. Crosses and filled circles denote the validated and the suspected flashes, respectively. Different colors denote association of the projectiles with active meteoroid streams. Image was taken from Liakos et al. (2024).

Using this dataset, empirical relationships were derived linking meteoroid mass to the peak magnitudes of the resulting LIFs (Fig. 9), offering a practical tool for estimating meteoroid masses in future observations, provided the same (*R* or *I*) filters are used. An important result from the analysis is the absence of correlation between meteoroid mass and impact temperature, regardless of impact location. Additionally, no significant correlation was found between meteoroid size and peak temperature, despite the potential influence of contact surface area. These findings suggest that the flash temperature is largely independent of, or possibly even anticorrelated with, the mass and size of the impacting projectile.

The distribution of peak temperatures for validated LIFs, along with estimated temperatures for suspected events, is shown in Fig. 10. A significant fraction (45.8%) of validated flashes exhibited peak temperatures between 2500 and 3500 K, while 84.9% fell within the 2000-4500 K range. Only 3.6% of events had peak temperatures below 2000 K, and 11.5% exceeded 4500 K. For suspected flashes, peak temperature estimates — derived from inferred *R*-band magnitudes — peak between 1500 and 2000 K and should be considered upper limits.

The derived meteoroid mass distribution, assuming a luminous efficiency of $\eta = 1.5 \times 10^{-3}$, is also presented in Fig. 10. The calculated masses range from ~2 g to ~2.7 kg, with the majority (60.4%) below 100 g and distributed evenly in 25 g bins. A total of 76.6% of meteoroids had masses less than 200 g, and 88% were under 400 g. As expected from the mass–magnitude relation, suspected LIFs are associated with significantly smaller masses, typically under 50 g. Corresponding projectile radii — again assuming $\eta = 1.5 \times 10^{-3}$ — ranged from 0.7 to 6.95 cm (Fig. 10). Most validated mete-

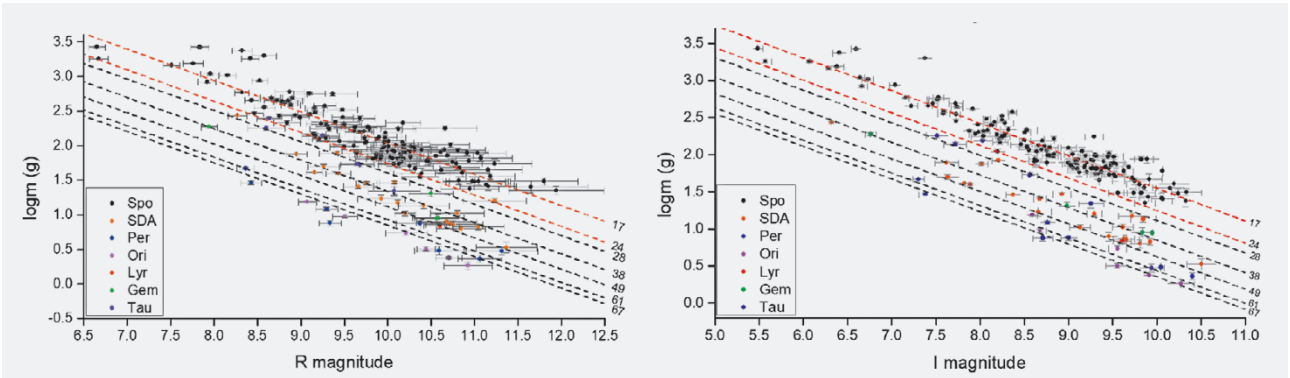

Figure 9. Correlations between peak magnitudes in *R* (left panel) and *I* (right panel) pass bands and meteoroid masses for η=1.5×10^{-3} (Liakos et al. 2024). The assumed velocities are indicated next to each fitting curve.

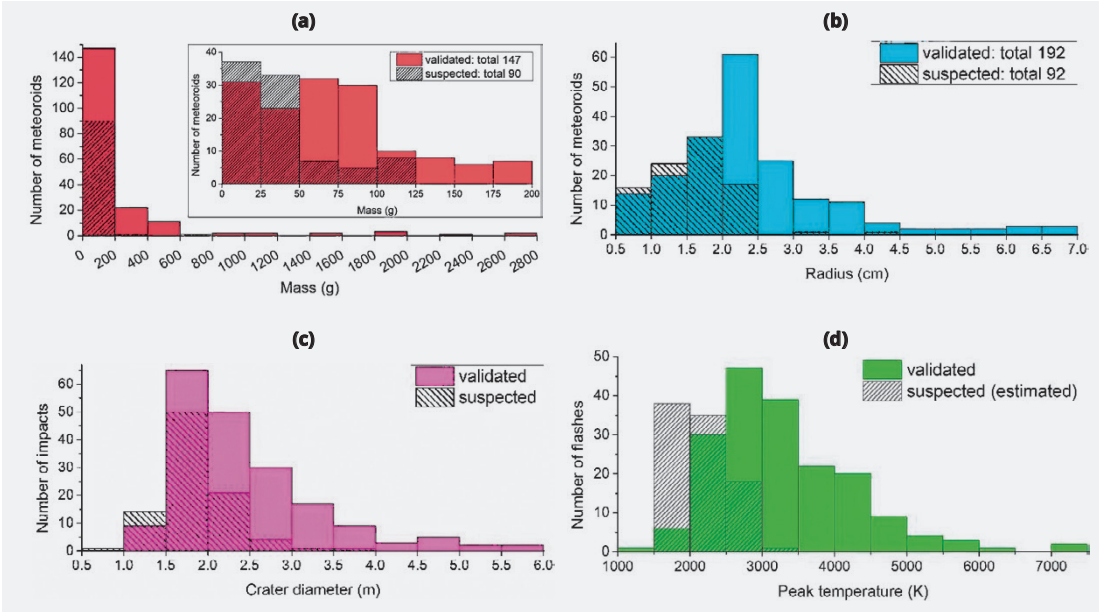

Figure 10. Distributions of masses (a) and radii (b) of the meteoroids, the peak temperatures of the impacts (c), and the dimensions of formed craters (d) as calculated from the analysis of lunar impact flashes from NELIOTA (Liakos et al. 2024).

oroids (69.8%) and nearly all suspected ones had radii less than 3 cm. For context, this size range spans from that of a two-euro coin (2.575 cm diameter) to a tennis ball (6.54 cm). Only 1.5% had radii under 2.8 cm (comparable to a one-euro coin), while 11.9% measured between a tennis ball and a baseball (6–8 cm), and just 4.1% approached the size of a shot-put sphere (~13 cm diameter). The associated kinetic energies of these meteoroids spanned 1–200 MJ. Using the Gault (1974) scaling law (see also Melosh 1989), crater sizes resulting from these impacts were estimated assuming a 45° impact angle. For validated flashes, crater diameters range from 1 to 6 m, with a pronounced peak between 1.5 and 2 m, also seen in the suspected events.

Assuming homogeneous meteoroid flux across the lunar surface — and by extension the Earth — appearance frequencies for both sporadic and stream-related meteoroids were extrapolated to lunar and near-Earth space (Fig. 11). These appearance rates were then used to estimate the probability of meteoroid impacts on hypothetical lunar infrastructure or satellites. The analysis considered varying target sizes, from a small structure (30 m^2) to a large facility the size of a football field (8000 m^2). The resulting probabilities, shown in Fig. 12, depend solely on the effective target area and the corresponding impact frequency, independent of orbital altitude.

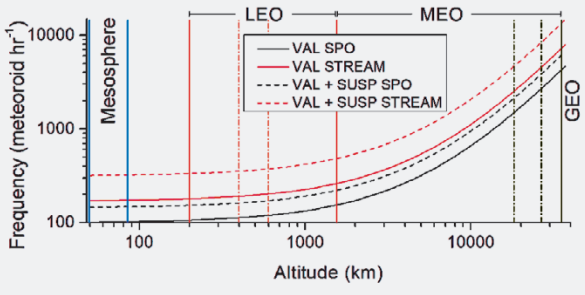

Figure 11. Appearance frequency distributions of meteoroids around Earth up to an altitude of 36000 km. Black and red lines denote the sporadic and the stream meteoroids, respectively. Solid lines correspond to the frequencies based on only the validated flashes, while dashed lines are those that are based on the validated and suspected flashes. Vertical solid lines indicate the boundaries of the mesosphere, LEO, MEO, and GEO zones. Vertical dashed lines indicate satellite crowed orbit zones. The image was taken from Liakos et al. (2024).

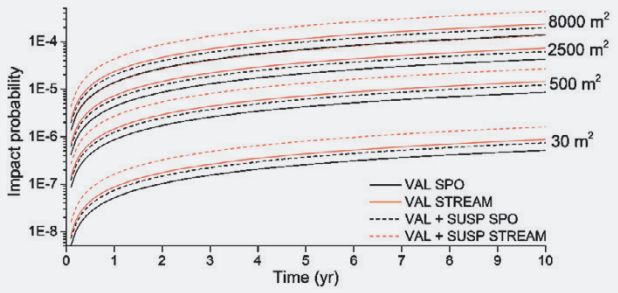

Figure 12. Impact probability of meteoroid with potential infrastructure on lunar surface or with a satellite in orbit around Earth for various impact surface areas (30 m^2 – small size building or satellite, 500 m^2, 2500 m^2 – medium size building or satellite, 10 000 m^2 – large size building or ISS size satellite). Colors and line styles denote the same as in Fig. 11. The image was taken from Liakos et al. (2024).

Discussion and future of LIFs

For 6.5 years, NELIOTA monitored the Moon for LIFs using the 1.2-meter Kryoneri telescope — currently the largest telescope in the world dedicated to this type of observations. This project stands as the longest-running systematic campaign for LIF detection to date, having produced a vast dataset exceeding 215 terabytes of lunar imagery. The large aperture of the Kryoneri telescope enabled the detection of LIFs up to two magnitudes fainter in the *R* band compared to previous efforts (e.g., the NASA Meteoroid Environment Office campaign). Additionally, the dual-band observational approach allowed for robust statistical analysis of the temperatures associated with meteoroid impacts.

Through its extended observational timeline and technological capabilities, NELIOTA has significantly advanced our understanding of both LIFs and corresponding meteoroids. Observations concluded in mid-August 2023 following the completion of the program's funding cycle. However, after the positive evaluation of a proposal submitted to the European Space Agency (ESA), the operations of the programme will resume within summer 2025 and will last for three years. In addition to continuing the monitoring campaign, we strongly advocate for establishing coordination between observers of meteors, fireballs, bolides, and LIFs — particularly during meteor showers. Such collaborative efforts would be especially valuable for constraining the luminous efficiency of LIFs, a key parameter in energy and mass calculations. Although the NELIOTA campaign has yielded a substantial dataset, further observations are essential, especially during peak meteoroid stream activity, to enhance the statistical robustness of our conclusions.

Looking ahead, the ESA-funded mission *Lunar Meteoroid Impact Observer* (LUMIO) is scheduled for launch in 2027 (Cipriano et al. 2018; Topputo et al. 2018, 2023). The authors of this article are actively involved in LUMIO as members of two working groups on the mission's science team. Like the NELIOTA system, LUMIO will employ a dual-camera setup with a dichroic beam splitter, observing in both the visible and near-infrared bands at a frame rate of 10–20 frames per second. It will monitor the dark side of the Moon for approximately 15 days per month, focusing on periods when lunar illumination is below 50%.

While LUMIO is expected to detect hundreds of LIFs, its position at the Earth–Moon L2 point does not fully resolve observational limitations associated with subradiant points of meteoroid streams. Moreover, due to its opposition geometry relative to Earth, LUMIO will observe the Moon during different lunar phases than those visible from ground-based stations. For these reasons, we emphasize that ground-based LIF monitoring from multiple geographical locations remains essential. Such efforts are not only complementary to LUMIO, but also critical for maintaining continuous coverage and resolving stream-related observational asymmetries.

References

Babadzhanov, P. B., & Kokhirova, G. I. 2009, A&A, 495, 353

Bellot Rubio, L. R., Ortiz, J. L., & Sada, P. V. 2000a, ApJ, 542, L65

Bellot Rubio, L. R., Ortiz, J. L., & Sada, P. V. 2000b, Earth Moon Planets, 82, 575

Bessell, M. S., Castelli, F., & Plez, B. 1998a, A&A, 337, 321

Bessell, M. S., Castelli, F., & Plez, B. 1998b, A&A, 333, 231

Bonanos, A. Z., Avdellidou, C., Liakos, A., et al. 2018, A&A, 612, A76

Bouley, S., Baratoux, D., Vaubaillon, J., et al. 2012, Icarus, 218, 115

Brown, P., Spalding, R. E., ReVelle, D. O., Tagliaferri, E., &Worden, S. P. 2002, Nature, 420, 294

Brown, P., Wong, D. K., Weryk, R. J., & Wiegert, P. 2010, Icarus, 207, 66

Cipriano, A. M., Dei Tos, D. A., & Topputo, F. 2018, Front. Astron. Space Sci., 5, 29

Gault, D. E. 1974, in A Primer in Lunar Geology, eds. R. Greeley, & P. H. Schultz

Hughes, D. W. 1987, A&A, 187, 879

Jenniskens, P. 1994, A&A, 287, 990 Liakos et al. 2020

Liakos, A., Bonanos, A. Z., Xilouris, E. M., et al. 2020, A&A, 633, 112

Liakos, A., Bonanos, A. Z., Xilouris, E. M., et al. 2024, A&A, 687, 14

Madiedo, J. M., Ortiz, J. L., & Morales, N. 2017, in Lunar Planet. Sci. Conf., 1319

Madiedo, J. M., Ortiz, J. L., Morales, N., & Cabrera-Caño, J. 2015a, Planet. Space Sci., 111, 105

Madiedo, J. M., Ortiz, J. L., Organero, F., et al. 2015b, A&A, 577, A118

Madiedo, J. M., Ortiz, J. L., & Morales, N. 2018, MNRAS, 480, 5010

Madiedo, J. M., Ortiz, J. L., Morales, N., Roman, A., & Alonso, S. 2019, in Lunar Planet. Sci. Conf., 1406

Melosh, H. J. 1989, Impact cratering: A Geologic Process (Oxford University Press)

Moser, D. E., Suggs, R. M., Swift, W. R., et al. 2011, in Meteoroids: The Smallest Solar System Bodies, eds. W. J. Cooke, D. E. Moser, B. F. Hardin, & D. Janches, 142

Ortiz, J. L., Aceituno, F. J., Quesada, J. A., et al. 2006, Icarus, 184, 319

Ortiz, J. L., Madiedo, J. M., Morales, N., Santos-Sanz, P., & Aceituno, F. J. 2015, MNRAS, 454, 344

Suggs, R. M., Moser, D. E., Cooke, W. J., & Suggs, R. J. 2014, Icarus, 238, 23

Swift, W. R., Moser, D. E., Suggs, R. M., & Cooke, W. J. 2011, in Meteoroids: The Smallest Solar System Bodies, eds. W. J. Cooke, D. E. Moser, B. F. Hardin, & D. Janches, 125

Topputo, F., Dei Tos, D. A., & Cipriano, A. 2018, in 42nd COSPAR Scientific Assembly, 42, PSD.1-28-18

Topputo, F., Merisio, G., Franzese, V., et al. 2023, Icarus, 389, 115213

Xilouris, E. M., Bonanos, A. Z., Bellas-Velidis, I., et al. 2018, A&A, 619, 141

Forecast of Actionable Radiation Belt Scenarios (FARBES)

by **Ioannis A. Daglis[1], Christos Katsavrias[1], Stavros Dimitrakoudis[1], Georgios Balasis[2,1], Adamantia Zoe Boutsi[1], Marina Georgiou[1], and Constantinos Papadimitriou[1]**

[1] *Department of Physics, National and Kapodistrian University of Athens*

[2] *IAASARS, National Observatory of Athens*

Introduction

The term "Space Weather" has gained a lot of publicity in recent years mainly because, in the general public, it is associated with disturbances in the Earth's magnetic field, the so-called "Geomagnetic Storms". However, space weather is an entire field of research into phenomena in the solar system caused by extraordinary solar activity (coronal mass ejections, flares, fast solar wind flows, interaction regions, etc.). This extraordinary solar activity (or solar storms) often leads to sequences of severe disturbances of the upper atmosphere and near-Earth space environment that can damage modern technology on the ground and in space (satellite systems, telecommunications, navigation systems, terrestrial power generation networks). Therefore, space weather prediction requires the detailed description of a system-of-systems, including the Sun, the solar wind and the Earth's magnetosphere [Kepko et al., 2024].

The past couple of decades, special interest has been given to the prediction of the variability of the outer radiation belt electron population. Radiation belts are torus-shaped plasma environments confined by planetary magnetic fields and which are continuously driven away from a state of local thermodynamical equilibrium due to energy-momentum deposition from the solar wind. Earth's radiation belts sustain a wide range of plasma instabilities that mimic collisions and thermalize the plasma. These plasma instabilities result in a broad spectrum of fluctuations that accelerate particles to relativistic energies on timescales of a few hours to a few days. With electron energies spanning almost seven orders of magnitude, and reaching as high as several MeV, the Earth's radiation belts are the closest natural laboratory, in which charged particles are accelerated close to the speed of light [Daglis et al., 2019].

From an applied physics perspective, radiation belt particles constitute a threat to satellites orbiting Earth due to their high energies and their confinement location near frequented satellite orbits. To give a sense of just how energetic these particles are, an electron with 1 MeV energy near geosynchronous orbit moves with a speed close to the speed of light; it completes an orbit around the planet, covering a total distance of approximately 240.000 km, in less than 20 minutes. These particles can be dangerous for human endeavours in space, causing damage to sensitive spacecraft components — rightly earning the reputation of "satellite killers" — and to biological tissue. Numerous works have investigated the effect of geospace disturbances and storms on the radiation belt electron population [Reeves et al., 2003; Turner et al., 2015; Katsavrias et al., 2019a]. Regardless of the individual results of these studies, all of them have argued that the outcome of a given geospace disturbance on the outer belt dynamics is the result of a delicate interplay of the various acceleration and loss mechanisms. Regarding acceleration, the most important mechanisms are inward radial diffusion via drift-resonance of electrons with Pc4-5 Ultra Low Frequency (ULF) waves (frequency range 1–22 mHz) or local acceleration of electrons via gyroresonance with whistler mode chorus waves (frequency range $0.1f_{ce}$ to $0.8f_{ce}$, where f_{ce} is the electron gyrofrequency). Several case studies [e.g. Li et al., 2016; Ma et al., 2016; Liu et al. 2018] have shown that the relative contribution of each mechanism to the electron energization is highly event specific and have, moreover, highlighted the energy–dependent radial extent of the electron population. On the other hand, Jaynes et al. [2015] proposed that ULF waves, through enhanced inward radial diffusion of relativistic electrons in the 1-2 MeV energy range, can lead to enhancement of several MeV electron fluxes. This scenario was, later, proved to be the acceleration mechanism of ultra-relativistic electrons (3-5 MeV energy range) during the mid-April of 2017 event [Katsavrias et al., 2019b]. From all the above, it is clear that the resulting electron acceleration, during each event with concurrent ULF and chorus activity, is the cumulative effect of local heating and inward radial diffusion. In addition, the relative contribution of the two mechanisms is possibly energy dependent.

The current state of the art in relativistic electron radiation belt models for operational needs come in two flavours — a "nowcast" based on data assimilation of relevant and timely measurements (such as used in Meteorology or Oceanography) into a physics based model, and limited "forecasts" based on statistical forecasts of indices or solar wind parameters that govern the dynamics in physical models. The preferred direction to follow would naturally be the logical chain of prediction, i.e., from the emergence of an unstable structure at the surface of the Sun, to its impact on the Earth's magnetosphere and its induced perturbations along commercial satellite orbits. Nevertheless, the prediction of solar dynamics, is still in an "embryonic state", while the provision of real time in situ measurements in key regions of the magnetosphere (as well as in the solar wind and close to the Sun) is something currently not available in Europe at all and limited to NOAA-GOES data at geosynchronous orbit only in the North America.

The FARBES project

In order to overcome these limitations, the FARBES project (https://www.farbes.eu/) aims at developing a framework that will allow the provision of actionable information on future high-energy electron ("killer electron") environments for spacecraft operators, based on easi-

ly sustainable ground-based drivers and measurements with the most-likely scenario based forecast of the radiation belt dynamics. The steps are as follows:

1. Accurate initial state specification of both environment and drivers using readily available real-time innovative ground-based input parameters, driving state-of-the-art diffusive radiation belt models (current now-cast).
2. Then the forecast methodology is based on prediction scenarios of subsequent behaviour of a few key quantities of interest to spacecraft operators:
   a. Time to most severe environment
   b. Most severe flux to be reached
   c. Time to the end of the on-going event
3. Finally, recursively evolve the predictions as the event unfolds using up-to-date initial conditions and drivers to update the scenario-based predictions.

The "current now-cast" is provided by the Salammbô radiation belt model [Beutier and Boscher, 1995]. The Salammbô model developed at ONERA belongs to this physics-based category and is mature enough to be used as a forecast tool. Indeed, all the physical processes acting and driving the dynamics of the radiation belts are taken into account and have recently been validated against Van Allen Probes, POES and GOES data. Nevertheless, its fidelity depends on the availability and accuracy of several inputs, such as: a) the outer boundary condition (magnetopause boundary and injected distribution from the plasma sheet), b) the background plasma density, c) the amplitudes of natural waves and their distribution (Chorus, Hiss, EMIC), d) the amplitude and distribution of radial diffusion coefficients and e) the low energy boundary condition. To that end, FARBES objectives include the provision of accurate inputs to drive the Salammbo model and produce prediction scenarios of the subsequent radiation belt behavior.

The FARBES objectives

In detail, FARBES objectives include:

- ***Specification of in-situ natural wave environment from ground based VLF data.*** Energetic electrons in the outer radiation belt can undergo gyro resonant interaction with various magnetospheric wave modes including whistler-mode VLF chorus outside the plasmasphere and whistler-mode hiss inside the plasmasphere. The result of this process can be energization and precipitation of the energetic electrons by pitch angle or energy scattering. The calculation of the corresponding diffusion coefficients requires the wave power of these waves at the wave-particle interaction region. This is available only for certain locations and times from in situ measurements of recent science missions (Van Allen Probes, ERG missions) and not in real-time. In Farbes, the derivation of the wave power will be based on comparison of measured in-situ and ground VLF wave power.
- ***Improved Radial Diffusion Coefficients for Radiation Belt Modelling.*** Aligned with the overall philosophy of the project, these are driven by data from ground sources which are expected to be available and maintained into the near term. Recently, it was shown how, especially at ultra-relativistic energies where the impacts of VLF chorus and hiss acceleration and loss are very slow [Mann et al., 2016], that the overall structure of the belt can be reproduced using accurate knowledge of the radial diffusion coefficients, D_{LL}. Whilst there are statistical models for D_{LL} which are available as functions of L (L*) and solar wind or geomagnetic indices such as Kp [e.g., Brautigam and Albert, 2000; Ozeke et al., 2014], a much better radiation diffusion specification can be obtained by using ground-based observations of ULF wave power and mapping it into the equatorial plane [e.g., Mann et al., 2016]. More specifically, radial diffusion can be broken down into separate terms stemming from either electric (or electrostatic) or magnetic (or electromagnetic, depending on the formulation) drivers. The electric term in space can be derived from measurements of the geomagnetic field on the ground, and this is the approach we follow here (following Ozeke et al. [2009] and Ozeke at al. [2012]). This normally requires several ground magnetometers spaced out in both longitude and latitude, but the FARBES nowcasting setup is limited to an almost meridional line that cuts across Europe from north to south (EMMA (European quasi-Meridional Magnetometer Array), from Norway to Italy, plus ENIGMA (HellENIc GeoMagnetic Array) in Greece). Considering previous observations on the coherence of ULF waves across different longitudes during storm times [Dimitrakoudis and Mann 2019] a statistical study was undertaken to quantify the expected longtitudinal difference in measurements for different local times, so that measurements from that line of magnetometers can be used for the continuous supply of D_{LL} values to models that require them.
- ***Validation of Radiation Belt model using ground-based drivers and Scenario-based predictions.*** The final step is to incorporate the improved VLF and ULF wave environment along with the appropriate initial and boundary conditions to infer the initial state of the forecast. Therefore, FARBES will address the challenge of improving the reliability of the proxies used to drive Salammbô by exploiting ground-based measurements, while also keeping an estimate of the uncertainty induced during simulations. Finally, the nowcast will be constantly refined during an event by the ongoing availability of real-time model inputs, thus overcoming the need for data assimilation using often unavailable in situ data.

The FARBES project has received funding from the European Union's Horizon Europe research and innovation programme under grant agreement No 101081772. It is a continuation of important previous efforts such as: the FP7-MAARBLE project (2011-2014), and the H2020-SafeSpace project (2020-2022), both led by the Space Physics Group of the National and Kapodistrian University of Athens.

References

Beutier and Boscher (1995). SALAMM-BO: A three-dimensional simulation of the proton radiation belt. JGR. Space Phys, 100(A9), pp. 17181–17188, doi: 10.1029/94JA02728

Brautigam, D. and J. Albert (2000), Radial diffusion analysis of outer radiation belt electrons during the October 9, 1990, magnetic storm, Journal of Geophysical Research, 105, 291-309.

Daglis, I.A. et al. (2019). From solar sneezing to killer electrons: Outer radiation belt response to solar eruptions. Phil. Trans. R. Soc. A 377 (2148), 20180097. doi:10.1098/rsta.2018.0097

Dimitrakoudis, S. and Mann, I.R. (2019) On the Close Correspondence between Storm-time ULF Wave Power and the POES VLF Chorus Wave Amplitude Proxy. Geophysical Research Letters, 46, 1947–1955, https://doi.org/10.1029/2018GL081317

Jaynes, A.N. et al. (2015). Source and seed populations for relativistic electrons: Their roles in radiation belt changes. JGR. Space Phys. 120, 7240–7254. doi:10.1002/2015JA021234

Katsavrias, C. et al. (2019a). On the statistics of acceleration and loss of relativistic electrons in the outer radiation belt: A superposed epoch analysis. JGR. Space Phys. 124, 2019JA026569–2768, doi:10.1029/2019JA026569

Katsavrias, C. et al (2019b). Highly relativistic electron flux enhancement during the weak geomagnetic storm of April–May 2017. JGR. Space Phys. 124, 4402–4413. doi:10.1029/2019JA026743

Kepko, L., et al (2024). Heliophysics Great Observatories and international cooperation in Heliophysics: An orchestrated framework for scientific advancement and discovery. Adv. Space Res. 73, 5383-5405, https://doi.org/10.1016/j.asr.2024.01.011

Li, W. et al. (2016). Radiation belt electron acceleration during the 17 March 2015 geomagnetic storm: Observations and simulations. JGR. Space Phys. 121, 5520–5536. doi:10.1002/2016JA022400

Liu, S. et al. (2018). Quantifying extremely rapid flux enhancements of radiation belt relativistic electrons associated with radial diffusion. Geophys. Res. Lett, 45, 1262–1270. doi:10.1002/2017GL076513

Ma, Q. et al. (2016). Simulation of energy-dependent electron diffusion processes in the Earths outer radiation belt. JGR. Space Phys. 121, 4217–4231. doi:10.1002/2016JA022507

Mann, I.R., Ozeke, L.G., Murphy, K.R., Claudepierre, S.G., Turner, D.L., Baker, D.N., Rae, I.J., Kale, A., Milling, D.K., Boyd, A.J. and Spence, H.E., 2016. Explaining the dynamics of the ultra-relativistic third Van Allen radiation belt. Nature Physics, 12, 978–983. doi:10.1038/nphys3799

Ozeke, L. G., I. R. Mann, and I. J. Rae (2009), Mapping guided Alfvén wave magnetic field amplitudes observed on the ground to equatorial electric field amplitudes in space, J. Geophys. Res., 114, A01214, doi:10.1029/2008JA013041.

Ozeke, L. G., I. R. Mann, K. R. Murphy, I. J. Rae, D. K. Milling, S. R. Elkington, A. A. Chan, and H. J. Singer (2012), ULF wave derived radiation belt radial diffusion coefficients, J. Geophys. Res., 117, A04222, doi:10.1029/2011JA017463.

Ozeke, L. G., I. R. Mann, K. R. Murphy, I. Jonathan Rae, and D. K. Milling (2014), Analytic expressions for ULF wave radiation belt radial diffusion coefficients, J. Geophys. Res. Space Physics, 119, doi:10.1002/2013JA019204

Reeves, G. D. et al. (2003). Acceleration and loss of relativistic electrons during geomagnetic storms, Geophys. Res. Lett., 30(10), 1529, doi:10.1029/2002GL016513

Turner, D. L. et al. (2015). The effects of geomagnetic storms on electrons in Earth's radiation belts. Geophys. Res. Lett. 42, 9176–9184, doi:10.1002/2015GL064747

Visit our website

http://www.helas.gr

The above web server contains information, both in greek and english, about the Hellenic Astronomical Society (Hel.A.S.), the major organization of professional astronomers in Greece. The Society was established in 1993, it has more than 250 members, and it follows the usual structure of most modern scientific societies. The web pages provide information and pointers to astronomy related material, useful to both professional and amateur astronomers in Greece. It contains a directory of all members of the Society, as well as an archive of all material published by the Society, including electronic newsletters, past issues of "Hipparchos", and proceedings of Conferences of Hel.A.S. The server is currently hosted by the University of Thessaloniki.

ASSESS – Episodic Mass Loss in Evolved Massive Stars: Key to Understanding the Explosive early Universe (9/2018 – 8/2024)

by **Alceste Bonanos**

Institute for Astronomy, Astrophysics, Space Applications and Remote Sensing, National Observatory of Athens

Multiple lines of evidence from both the massive star and supernova communities are pointing to violent, episodic mass-loss events being responsible for removing a large part of the envelope of massive stars, especially in low-metallicity galaxies. Episodic mass loss, however, is not understood theoretically, neither accounted for in state-of-the-art models of stellar evolution, which has far-reaching consequences for many areas of astronomy. The goal of ASSESS was to determine the role of episodic mass loss in the evolution of the most massive stars by conducting the first extensive, multi-wavelength survey of evolved massive stars in the nearby Universe. The target selection was based on the fact that mass-losing stars form dust and are bright in the mid-infrared. ASSESS aimed to (i) derive physical parameters of a large sample of dusty, evolved massive stars and estimate the amount of ejected mass, (ii) constrain evolutionary models, (iii) quantify the duration and frequency of episodic mass loss as a function of metallicity.

ASSESS developed a photometric classifier, i.e. a machine-learning algorithm, based on existing multi-band photometry and applied it to luminous sources in ~26 nearby galaxies, yielding reliable classifications of over 275,000 dusty sources in 21 nearby galaxies[1,2]. ASSESS also conducted a large spectroscopic survey of dusty, evolved stars in nearby galaxies spanning a range of metallicity, resulting in the largest catalog of evolved massive stars (185 stars) beyond the Local Group[3,4], including 129 low-metallicity red supergiants, 3 new luminous blue variables and 6 new supergiant B[e] stars[5]. We investigated the different temperature scales of RSG, i.e. those based on TiO lines measured in the optical vs. atomic lines measured in the near-IR and derived a scaling relation that translates one to the other. We also found substantial changes in

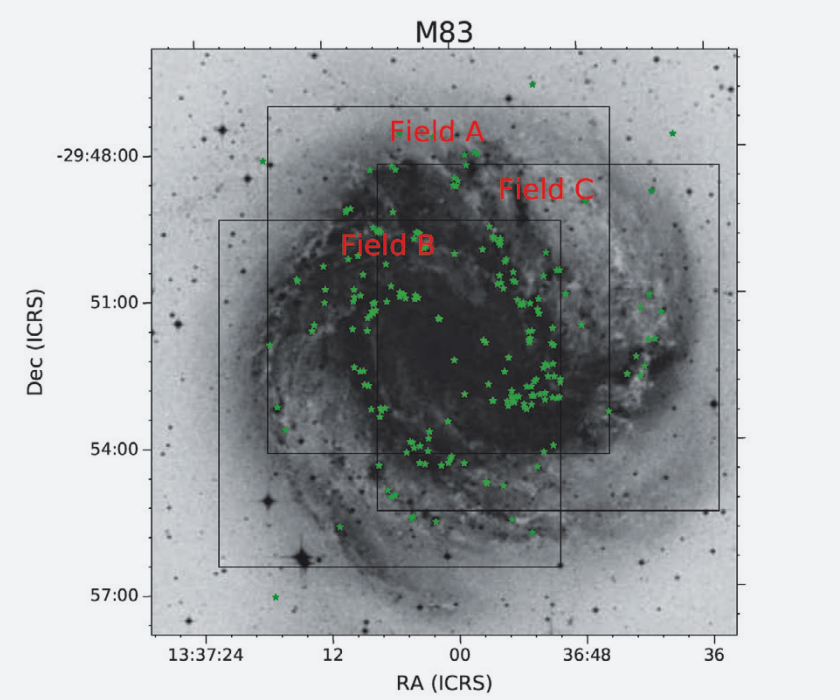

Figure 1: ASSESS fields and priority tagets (green stars) in M83, observed with the VLT.

Figure 2: ASSESS team members in June 2023 (L to R). *Front row*: Stephan de Wit, Evangelia Christodoulou, Alceste Bonanos, Stella Avgousti. *Back row*: Gonzalo Munoz-Sanchez, Grigoris Maravelias, Kostas Antoniadis, Manos Zapartas.

the spectral types (i.e. effective temperatures) of >10% of our RSGs[6], providing evidence for episodic mass loss and an estimate on the occurrence rate.

ASSESS for the first time measured precise and accurate mass-loss rates using the largest-ever sample of red supergiants in the Magellanic Clouds[7,8], finding enhanced mass loss at luminosities above log(L/Lo)~4.5, and lower rates by 2-3 orders of magnitude, compared to the mass-loss relations applied in evolutionary models. Furthermore, we applied four empirical mass-loss rate prescriptions to stellar evolutionary models and found that no prescription can explain all the observational constraints for red supergiants[9]. We highlight the extreme (in luminosity and radius) red supergiant [W60] B90[10] in the Large Magellanic Cloud (LMC), which is a massive analog of Betelgeuse, exhibiting 3 dimming events, as well as evidence for a bow shock[11]. Finally, we discovered that WOH G64, a red supergiant in the LMC boasting the highest luminosity and mass-loss rate, underwent a never-seen before transition to the blue in 2013-2014[12], which has implications for the 'red supergiant problem' and the Humphreys-Davidson limit.

The ASSESS team has been awarded 44 h on FORS2/VLT to obtain spectra of over 900 stars in ten southern galaxies and 67 h (partially completed) on OSIRIS/GTC to obtain spectra of 90 priority stars in 3 northern galaxies. The catalogs of massive stars and their properties are publically available. We also obtained observations with the Magellan telescopes over 10 hours and with EMIR/GTC to investigate the temperature scale and spectral variability of luminous and dusty red supergiants. The results of this project were presented in 41 scientific publications (36 of which are in peer-reviewed journals and 5 are conference proceedings), 15 conferences, 11 workshops and 6 seminars.

ASSESS has advanced our knowledge of episodic mass loss beyond the state of the art:

- The machine-learning photometric classifier that we have developed is novel and its application has yielded a dataset that will be very valuable for research within the massive star community and beyond.
- The newly derived mass-loss rates for red supergiants are extremely valuable for producing accurate stellar evolution models. We expect that our new mass-loss prescription for red supergiants will be widely used.
- The detailed study of two extreme red supergiants has provided great insight and advanced our knowledge for these objects, paving a way forward to understanding the physics governing these extreme evolutionary states.
- The catalogs of spectroscopically classified massive stars in both southern and northern galaxies are made available to the community for further use.

References

1. Maravelias, G. et al. 2022, A&A, A machine-learning photometric classifier for massive stars in nearby galaxies. I. The method, 666, 122, doi:10.1051/0004-6361/202141397
2. Maravelias, G. et al. 2025, A&A subm., A machine-learning photometric classifier for massive stars in nearby galaxies II. The catalog (arXiv:2504.01232)
3. Bonanos, A. et al. 2024, A&A, Investigating episodic mass loss in evolved massive stars. I. Spectroscopy of dusty massive stars in ten southern galaxies, 686, 77, doi:10.1051/0004-6361/202348527
4. de Wit, S. et al. 2025, A&A, in press, Investigating episodic mass loss in evolved massive stars: III. Spectroscopy of dusty massive stars in three northern galaxies (arXiv:2505.01498)
5. Maravelias, G. et al. 2023, Galaxies, Discovering New B[e] Supergiants and Candidate Luminous Blue Variables in Nearby Galaxies, 11, 3, doi:10.3390/galaxies11030079
6. de Wit, S. et al. 2024, A&A, Investigating episodic mass loss in evolved massive stars: II. Physical properties of red supergiants at subsolar metallicity, 689,46, doi:10.1051/0004-6361/202449607
7. Yang, M. et al. 2023, A&A, Evolved massive stars at low-metallicity. V. Mass-loss rate of red supergiant stars in the Small Magellanic Cloud, 676, 84, doi:10.1051/0004-6361/202244770
8. Antoniadis, K. et al. 2024, A&A, Establishing a mass-loss rate relation for red supergiants in the Large Magellanic Cloud, 686, 88, doi:10.1051/0004-6361/202449383
9. Zapartas, E. et al. 2025, A&A, The effect of mass loss in models of red supergiants in the Small Magellanic Cloud, 697, 167, doi:10.1051/0004-6361/202452401
10. de Wit, S. et al. 2023, A&A, Properties of luminous red supergiant stars in the Magellanic Clouds, 669, 86, doi:10.1051/0004-6361/202243394
11. Munoz-Sanchez et al. 2024, A&A, Episodic mass loss in the very luminous red supergiant [W60] B90 in the Large Magellanic Cloud, 690, 99, doi:10.1051/0004-6361/202450737
12. Munoz-Sanchez et al., subm., The dramatic transition of the extreme Red Supergiant WOH G64 to a Yellow Hypergiant (arXiv:2411.19329)

Six Years Through the Galactic Veil: PASIPHAE's Breakthrough Moment

by **Konstantinos Tassis**

University of Crete and IA-FORTH

Six years ago, PASIPHAE began as a bold idea: map the magnetic skeleton of our galaxy by decoding the polarization of starlight. Today, it stands on the brink of delivering on that promise. Funded in part by a European Research Council Consolidator Grant which concluded in May 2024 and a grant by the Stavros Niarchos Foundation, PASIPHAE (Polar-Areas Stellar-Imaging in Polarization High-Accuracy Experiment)[1] is now entering its most ambitious phase. A global collaboration — spanning Greece, India, the U.S., South Africa, and Norway — has built the tools, the algorithms, and the infrastructure needed to chart the Milky Way's invisible magnetic highways. The wide-field polarimeters (WALOPs), now in final testing[2], will go on-sky this year at observatories in Crete and South Africa. When they do, they will deliver high-accuracy measurements of stellar polarization across vast swaths of the northern and southern sky.

PASIPHAE isn't just building instruments. The team has already completed a full suite of data-processing algorithms[3], released an open-source toolkit for 3D magnetic field tomography[4], and developed a legacy catalog of high-precision stellar polarimetric standards[5]. The first map — covering a region 15 times the area of the full Moon — offers the most detailed three-dimensional reconstruction of Galactic magnetic fields ever assembled[6].

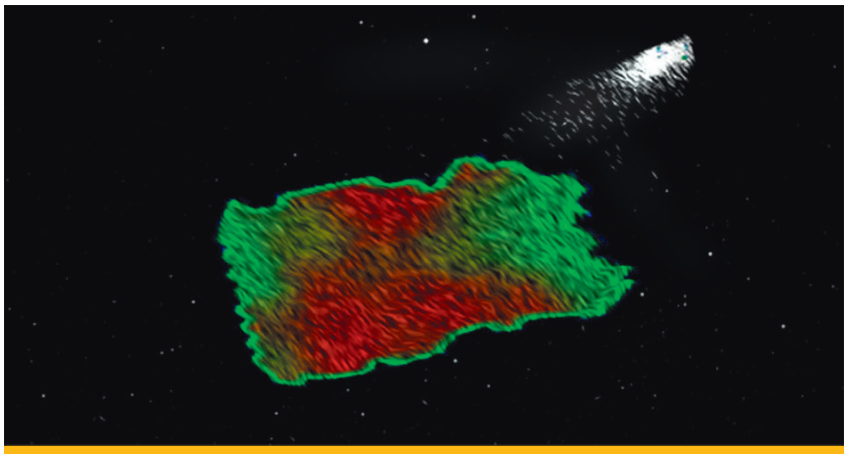

Figure: First 3D tomographic map of the Galactic magnetic field from PASIPHAE pilot observations.

An interactive visualization webpage (https://pasiphae.science/visualization) now allows users to fly through these mapped regions, exploring stars, dust clouds, and their magnetic threads in full three-dimensional context. It's a new way of seeing the Milky Way — not as a flat field of stars, but as a layered, dynamic medium shaped by magnetic forces.

This breakthrough matters far beyond our Galaxy. Polarized dust masks the faint signal of the cosmic microwave background (CMB), the afterglow of the Big Bang. PASIPHAE's 3D maps promise to peel back that Galactic veil, bringing us closer to detecting the CMB's polarized fingerprint — a potential key to understanding cosmic inflation and the laws of gravity at the Universe's birth[7].

The groundwork is laid. The technology is real. The veil is lifting.

1. https://pasiphae.science/

2. – Maharana, S. et al. 2021, Journal of Astronomical Telescopes, Instruments, and Systems, "WALOP-South: a four-camera one-shot imaging polarimeter for PASIPHAE survey. Paper I - optical design, 7, 014004. doi:10.1117/1.JATIS.7.1.014004
   – Maharana, S. et al. 2022, Journal of Astronomical Telescopes, Instruments, and Systems, WALOP-South: a four-camera one-shot imaging polarimeter for PASIPHAE survey. Paper II - polarimetric modeling and calibration, 8, 038004. doi:10.1117/1.JATIS.8.3.038004
   – Kypriotakis, J. A et al. 2024, Journal of Astronomical Telescopes, Instruments, and Systems, Wide Area Linear Optical Polarimeter North instrument I: optical design, filter design, and calibration, 10, 044005. doi:10.1117/1.JATIS.10.4.044005

3. Pelgrims, V. et al. 2023, A&A, Starlight-polarization-based tomography of the magnetized ISM: PASIPHAE's line-of-sight inversion method, 670, A164. doi:10.1051/0004-6361/202244625

4. https://github.com/vpelgrims/Bisp_1

5. Blinov, D. et al. 2023, A&A, The RoboPol sample of optical polarimetric standards, 677, A144. doi:10.1051/0004-6361/202346778

6. Pelgrims, V. et al. 2024, A&A, The first degree-scale starlight-polarization-based tomography map of the magnetized interstellar medium, 684, A162. doi:10.1051/0004-6361/202349015

7. – Ramaprakash, A., Readhead, A.~C.~S., & Tassis, K. 2021, Nature Astronomy, Lifting the dusty veil over inflation, 5, 519. doi:10.1038/s41550-021-01369-1
   – Tassis, K., et al. 2018, PASIPHAE: A high-Galactic-latitude, high-accuracy optopolarimetric survey, arXiv:1810.05652

The 17th Hellenic Astronomical Conference

The Hellenic Astronomical Conference, organized by the Hellenic Astronomical Society (Hel.A.S.), is the major scientific event of the greek astronomical community. The Conference, which takes place every two years in a different part of Greece, typically brings together over 100 scientists with research interests in Astrophysics, Planetary Science and Space Physics.

The 17th Conference of Hel.A.S. will take place in Patras, from June 30 to July 2 2025.

Invited plenary speakers (confirmed):

- **Didier Queloz**
  Professor of Physics at the Cavendish Laboratory, University of Cambridge, UK / EHT Zurich – Nobel Prize in Physics 2019
- **Dimitrios Psaltis**
  (J. H. Seiradakis Lecturer), Professor of Physics at the Georgia Institute of Technology
- **Iannis Dandouras**
  Director of Research, CNRS, Toulouse, Midi-Pyrénées
- **Andy Bunker**
  Professor of Astrophysics at the University of Oxford
- **Marica Branchesi**
  Professor of Physics at the Gran Sasso Science Institute, Department of Astroparticle Physics, L'Aquila, Italy

Back issues of Hipparchos

Hipparchos is the official newsletter of the Hellenic Astronomical Society. It is distributed by post to the members of the society. You can download back issues from: **http://www.helas.gr/news.php**